FACULTY OF MATHEMATICS AND PHYSICS
Charles University

DOCTORAL THESIS

David Babuka

Self-assembled polymer systems responsive to external stimuli for biomedicine

Institute of Macromolecular Chemistry CAS

Supervisor of the doctoral thesis: RNDr. Petr Štěpánek, DrSc.

Study programme: Physics

Study branch: Biophysics, Chemical and Macromolecular Physics

Prague 2022

Acknowledgment

Title: Self-assembled polymer systems responsive to external stimuli for biomedicine

Author: David Babuka

Department: Institute of Macromolecular Chemistry CAS

Supervisor: RNDr. Petr Štěpánek, DrSc., Institute of Macromolecular Chemistry CAS

Abstract: Stimuli-responsive self-assembled polymer nanoparticles are becoming increasingly more important tools in nanomedicine. In this thesis we studied two large sets of polymer samples designed to be capable of such self-assembly. Polymers in the first set, containing poly(2-methyl-2-oxazoline) or poly[*N*-(2-hydroxypropyl) methacrylamide] hydrophilic blocks and poly[*N*-(2,2-difluoroethyl)acrylamide] thermoresponsive block, were designed to act as ^{19}F MRI contrast agents. Polymers in the second set were designed as drug delivery systems and were based on 2-methyl-2-oxazine for hydrophilic parts and 2-propyl-2-oxazoline for thermoresponsive or 2-butyl-2-oxazoline for hydrophobic parts. Both sets of copolymers were prepared with various ratios of monomers in their blocks and the second set was also prepared with gradient chain architecture. Properties of their self-assembled systems were studied in detail and compared with regard to their potential for biomedical applications. The primary used method of analysis was dynamic light scattering supported by a vast array of methods including static light scattering, small angle X-ray and neutron scattering, nuclear magnetic resonance and others. From the investigated copolymers the most promising candidates for biomedical applications were selected and highlighted.

Keywords: light scattering, self-assembly, block copolymers, gradient copolymers, biomaterials

Contents

1 Foreword

Due to their unique properties, nanomaterials are becoming a standard compound of many different products. From protective coatings, paints and varnishes, [1] through cosmetic creams and shampoos, [2] to drug formulations for medicine. [3] They have been intensely researched in the past decades and the need for new and more complex nanomaterials is only growing. This also inevitably leads to the need for new advanced ways to prepare and analyse them. The nanomaterials can be both of inorganic origin, mainly conductive and semi-conductive metals and their oxides, as well as organic in nature, from small amphiphilic molecules to polymers. Especially polymers with their vast variability have proven to be very promising when researching new nanomaterials for biomedical applications. Many polymers are naturally found in living organisms so by taking inspiration from them new synthetic, biocompatible and biodegradable polymers can be designed and also imbued with other functionalities, such as self-assembly into nanostructures. These polymers can then be used to carry therapeutic or diagnostic compounds in the body for specific applications as they can target specific parts of the body helping to treat inflamed areas, [4, 5] sites of new implants, they can be used for ocular therapy, [6] neurodegenerative therapy, [7, 8] respiratory system therapy [9] and even for targeting certain cancerous tumours. [10-12] Of course, applications as sensitive as medical treatment of human body require the highest level of control over the properties of the polymers because every step of their preparation, from synthesis to application, can introduce deviations from the intended behaviour. To prevent this and ensure the properties of the materials are maintained, the polymers and their self-assembled nanoparticles can be analysed by a wide array of methods. Among these, the light scattering methods are proving to be very powerful as they are non-destructive, fast and provide statistically relevant information about the sample. [13] This work is focused on advanced analysis of newly designed self-assembled stimuli-responsive polymer nanoparticles for biomedical applications by physical methods, focusing primarily on the light scattering techniques.

2 Introduction

Nanomaterials have many properties different from bulk materials which can be used with advantage for biomedical purposes. One of the obstacles in our desire to utilize the nanomaterials is how to obtain them. There are generally two ways to approach this. One is a top-down approach in which we obtain the desired material from a larger object and the other is a bottom-up approach in which we obtain the desired nanoobject by assembly (usually self-assembly) of even smaller building blocks. [14] There are of course various methods of obtaining nanomaterials in both top-down as well as bottom-up approach, each with its unique properties, advantages and disadvantages. Among these the polymer self-assembly has proven to be quite a strong and versatile method especially as the self-assembly is directly inspired by processes intrinsic for existence of life and allows us to produce well defined nanoparticles of uniform sizes and even functionalities.

2.1 Macromolecules and self-assembly

2.1.1 Origins of self-assembly

Self-assembly as a physical process is an integral part of life as many biological processes depend on it, from double helix of DNA, through protein folding to cell membrane cohesion. So, as in many cases, the research attempts to learn from nature and copy these processes to unlock new possibilities. [15]

Self-assembly is a process in which a disorganized system of individual components transforms into an organized system. This change is driven by specific local interactions of the environment and the individual components without additional external influences. The basis of this are the electromagnetic forces acting between the present atoms, molecules and particles. These forces can be categorized and differentiated as they have various origins and effects in the observed systems.

On this scale the covalent bonds between atoms forming individual molecules can be considered short range and strong as their bond energies are typically in hundreds of kJ per mol and their length is typically 1-2 Å. These are responsible for keeping molecules and their parts with different properties, such as hydrophilic and hydrophobic, together.

On the other hand, we can consider the non-covalent interactions as long range and weak as their bond strength is typically 0.4-40 kJ·mol^{-1} and their interaction length is usually 2-100 Å or even more. [14, 15] Among these non-covalent interactions which can act intermolecularly as well as intramolecularly we can list electrostatic Coulomb interaction, van der Waals forces, hydrogen bonding, etc. [14-18]

Presence and prominence of these forces depends on chemical composition of the molecules and environment they are in. Some of the forces are attractive while others act repulsively which can also depend on distance between the interacting moieties. The balance between them is what determines the final size and morphology of the self-assembled system. [15]

The Coulomb electrostatic interaction is an attractive or repulsive force based on the charge of interacting particles and is prominent especially in molecules carrying an inherent charge.

The van der Waals forces are weak forces responsible for small molecular cohesion. They are attractive at longer distances (up to 6 Å) and repulsive below distances shorter than 4 Å. They are based on the interaction of permanent dipoles, induced dipoles and their cross-interactions.

Hydrogen bond is an effect specifically relating to a hydrogen atom which is being robbed of its electron density by a significantly more electronegative atom such as oxygen (O), fluorine (F) or nitrogen (N), effectively creating a partial positive charge on the hydrogen atom, which can then be attracted to a negative charge on a different atom. This interaction is of special importance in aqueous environment as water molecules spontaneously from a network interconnected by these hydrogen bonds and so they can also form hydrogen bonds with other present molecules if they possess appropriate bonding sites. The effect of the hydrogen bonds can be cumulatively so strong they cause that water has a boiling point at 100°C which is much higher than all the other hydrides from group 16 of the periodic table. [19] In aqueous solutions which are most appropriate for biomedical applications, as almost 60% of human body mass is formed by water, the hydrogen bonding is ever-present.

In the aqueous environment the result of all the acting forces discussed above is the hydrophobic interaction. It is best described on the basis of minimizing the free energy of the system of hydrophobic solute in aqueous environment. By aggregation of small hydrophobic units to larger particles their contact with water molecules is

minimized leading to overall decrease in the Gibb's free energy of the system. [20] This will be discussed further after we consider, what kind of hydrophobic solutes we will be working with.

2.1.2 Amphiphilic copolymers

At the beginnings of the research the self-assembly has been studied for small amphiphilic molecules in water. These molecules have a distinct hydrophilic and a hydrophobic part (see **Figure 1**) and are represented by systems as common as soaps and detergents.

Hydrophobic tail   Hydrophilic head
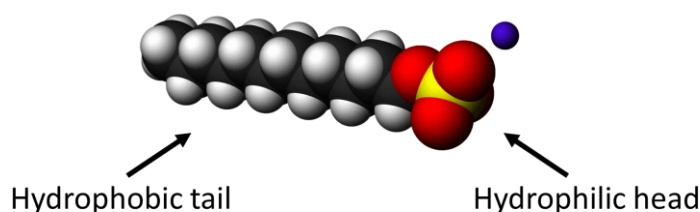
***Figure 1** Space-filling model of the sodium dodecyl sulfate as an example of small amphiphilic molecule. Adapted from [21].*

With development of polymer science, it was found that large molecules and especially block copolymers can exhibit self-assembly behaviour as well.

Polymers, composed of many building blocks interconnected by chemical bonds, can be classified by many different criteria. If classified by composition we can differentiate homopolymers, consisting of only one type of monomer, and copolymers, consisting of two or more different types of monomers. Copolymers can then be further classified according to their internal structure and how the different monomers are arranged in their molecules. Some examples are depicted in **Figure 2**.

Of special interest for us are the block and gradient architectures. Block copolymers have their monomers separated into two distinct blocks each consisting of a single type of monomer. Meanwhile monomeric composition of gradient copolymers gradually changes from one type of monomer to the other across the length of their molecular chain. This causes that both of these copolymer types have distinctly different physicochemical properties on the opposing ends of their chains dictated primarily by the type of monomer prevalent on the respective side.

- Random
- Alternating
- Block
- Gradient
- Graft
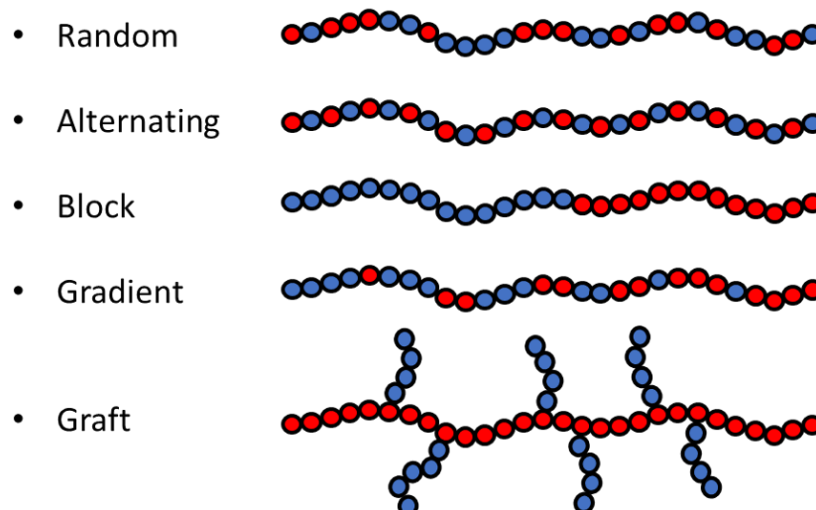
Figure 2 *Examples of copolymer internal architectures. The blue and red spheres represent monomers of two different types arranged in several different ways inside the copolymer chains.*

In analogy to the small amphiphilic molecules, it is then easy to imagine that block copolymers whose blocks would have opposing hydrophilic and hydrophobic properties might behave similarly and exhibit self-assembly behaviour.

Indeed, self-assembly of block copolymers in bulk has been studied in detail for more than 50 years. As such it is thoroughly explored. [22] However, the self-assembly of block copolymers in aqueous solutions which is much more relevant to biomedical applications, has only been studied with greater intensity since 1995. [23-26] This research has led to a significant expansion in the field of polymer science and since then many different block copolymers have been studied and more are developed every year.

A great advantage of polymers is their vast variability which leads to almost endless possibilities in preparation of new polymer systems. The properties of block copolymers can be also tuned by changing the ratio of lengths of their blocks to fit the desired applications. However, alongside their advantages they present some disadvantages as well. The multistep preparation necessary for their synthesis leads to difficult replication of the process as even minor variations in any of the steps propagates to the following steps and leads to structural variation between preparations even for simple diblock systems.

This obstacle can be avoided for analogous amphiphilic copolymers with gradient architecture which can be prepared by a one-pot statistical copolymerization of both monomers, in which case the gradient of monomers across the polymer chain

7

arises due to the differences in monomer reactivity. [27-36] This method allows the synthesis to have greater reproducibility and offers substantial financial and time savings when compared to the preparation of block copolymers. As such it is curious to note that there was not as much research done into their use and applications as for the block copolymers. [27]

2.1.3 *Self-assembly behaviour of copolymers*

The self-assembly of macromolecules in solution depends both on the polymers and solvents. The more complex the system the more complex the process of self-assembly. [23] The process of self-assembly is usually triggered by some change in the system, such as addition of different solvent, change of temperature etc. If the changes in the system are slow enough and the polymer chains have time to continuously equilibrate the system is under thermodynamic control and the resulting particle morphologies are path-independent and are determined by composition of the system and/or temperature. However, if the changes in the system are too large or too fast then the polymer chains do not have time to relax and the result of self-assembly can be dependent on the preparation pathway. In such a case the process is controlled kinetically and the particles are kinetically frozen. [23] So apart from the properties of the used polymers and solvents the preparation procedure can also have influence on the resulting morphology and size of the self-assembled system. [14]

From the factors affecting the self-assembly the most notable are the copolymer composition and concentration, amounts of common and selective solvents and their properties and presence of additional compounds such as salts, homopolymers etc. [23]

Generally speaking, the self-assembly of block copolymers in solution is caused by the long-range repulsive interactions which are based on the different miscibility of the two polymer blocks with the solvents and the short-range attractive interactions which are based on covalent bonds between the two blocks forcing them to stay together. [14] This creates a need for a part of the copolymer to phase separate from the surrounding solution. This need can be evaluated based on minimization of free energy of the system. [37] If we look at the self-assembly of polymer chains from the viewpoint of order (entropy) and chemico-physical interactions (enthalpy) then the self-assembly process causes the entropy of the individual chains in solvent to decrease as more organised particles are formed but is enthalpically favourable as it diminishes

the hydrophobe-water interaction thus decreasing the total free energy of the system ($\Delta G < 0$). This is characteristic for polymers in selective solvents and can be considered through Flory-Huggins solution theory which approaches thermodynamics of polymers in solution as a lattice model which helps to account for the difference in size of different present entities.

The interaction energies contributing to the energy of the system through the enthalpic term arise between individual polymer blocks, between molecules of solvent, as well as between the polymer blocks and solvent. [37] From these we get the interaction parameter χ, which helps to describe the phase behaviour of the system and is given by Flory-Huggins relation

$$\chi = \frac{a}{T} + b \tag{1}$$

where a and b terms depend on the actual polymer-polymer and polymer-solvent pairs and T is the absolute temperature. [14]

When considering real polymer solutions, the limitations of the Flory-Huggins model crop up and it is necessary to add another term χ_S into the **Equation 1** which describes all the remaining interactions in the system including the changes caused by varying temperature and effects of other interactions such as hydrogen bonding etc. Thus, we obtain equation

$$\chi = \frac{a}{T} + b + \chi_S \tag{2}.$$

The important observation from this equation and experimental practice is that the χ_S term can become dominant and direct the phase separation of the copolymers from the bulk solution, which exhibits as a responsive behaviour of the polymers on certain external stimuli. [14] This is of course very useful in polymers which are designed to self-assemble or disassemble at specific conditions.

The interaction parameter and the resulting shape of the self-assembled polymer system is determined mainly by relative volume fractions of the polymer blocks, their hydrophobicity and hydrophilicity and the length of the polymer chains as described by the degree of polymerization. This can be compared to packing parameter which is characteristic for small molecule surfactant micelles. [13, 14, 38] The packing parameter p for small amphiphilic molecules, such as surfactants, can be defined as

$$p = \frac{v}{a_0 l_c} \tag{3}$$

where v is the volume of the hydrophobic part of the molecule, a_0 is the area taken up by the head group, and l_c is the length of the hydrophobic tail of the surfactant molecule, as depicted in **Figure 3**.
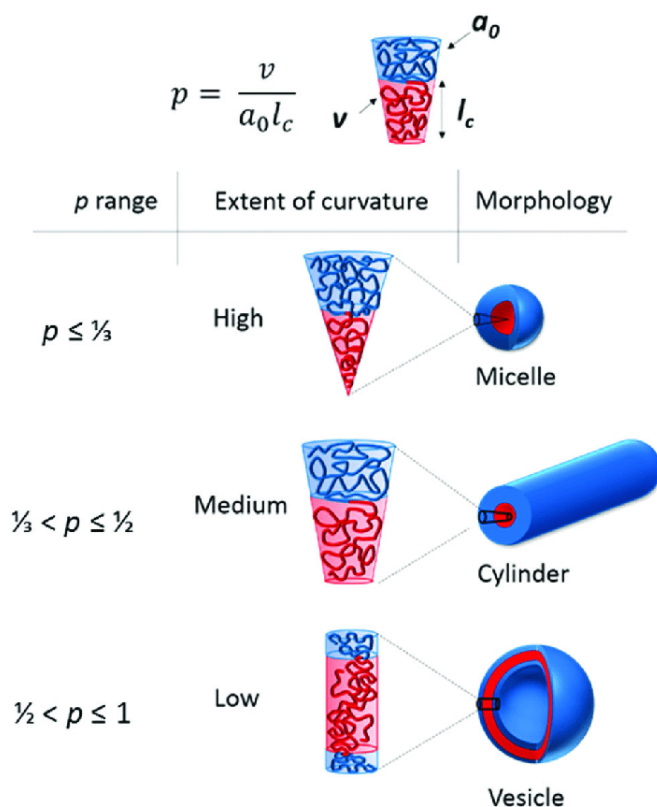
Figure 3 *The effect of different packing parameters on the resulting morphology of self-assembled system. [13]*

Based on the packing parameter a final shape of the self-assembled particle formed by a specific small amphiphilic molecule can be estimated. For $p \leq \frac{1}{3}$ spherical micelles are formed as they possess the highest curvature. For $\frac{1}{3} < p \leq \frac{1}{2}$ cylindrical micelles are formed, as their curvature is generally lesser than for their spherical counterparts. And for $\frac{1}{2} < p \leq 1$ particles with lowest curvature are formed such as bilayers or vesicles. It should be of course noted that any reasonable estimations from the packing parameter pertaining to the architecture of obtained nanoparticles extends only to the systems which are not kinetically frozen. [13]

In practice, packing parameter for polymers is very difficult or impossible to calculate and so when considering amphiphilic polymers, the volume fractions or mass

fractions of the hydrophilic and hydrophobic blocks are more commonly used for particle shape estimation. [13, 39] The ratio of volumes of hydrophilic and hydrophobic parts of the molecule significantly influences the resulting structure of the self-assembled particles. The block copolymers in solution of solvent selective for one of the blocks can assemble into various morphologies depending on the properties of the system constituents. Among the most common morphologies are spherical micelles, rods, also known as cylindrical or wormlike micelles, bicontinuous rods, layered structures such as bilayers, lamellae or vesicles, large compound micelles and nanogels. [14, 23]

Based on this it is possible to attempt to target specific morphologies by altering the chain lengths of individual blocks of the polymer or altering hydrophobicity of the blocks by using specific monomeric units. From synthesis to final self-assembly this process needs to be carefully controlled to obtain the desired size and morphology of resulting particles. [14] This is not trivial to achieve, as it is very difficult to maintain precise control over the polymer chain lengths and composition during the synthesis. Even though laboratory techniques are ever evolving and improving the results of synthesis and nanoparticle preparation still need to be carefully checked by analytical methods such as size exclusion chromatography (SEC) coupled with multi-angle light scattering (MALS), dynamic light scattering (DLS), small angle X-ray or neutron scattering (SAXS, SANS), nuclear magnetic resonance (NMR) spectroscopy of carbon (^{13}C) and hydrogen (^{1}H) atoms, and others. [13] The more precise the control over the whole process is the more reliable are the resulting properties of the self-assembled particles.

2.1.4 Dynamics of self-assembled systems and critical association concentration

The self-assembled polymer systems in solution usually exist in dynamic equilibrium between the unimers, freely dissolved as individual polymer chains, and the particles formed by them. This equilibrium is characterised by constant exchange of unimers between the particles and the bulk solution. [40] This process is fast and one event, when a polymer chain gets in or out of a particle, occurs every few microseconds. Simultaneously however particles are constantly disassembling and reassembling, this process takes significantly more time and is considered slow, as it

happens on the order of milliseconds. [14, 17] These dynamic processes apply only if the system is not kinetically frozen, as described above.

This process of constant self-assembly and disassembly is connected to another term and that is the critical association concentration (CAC). This is the concentration of polymer in solution below which essentially all the polymer chains are unimolecularly dissolved and are not assembled into micelles or other supramolecular structures. Above this concentration all the excess polymer additionally dissolved in the solution goes into the supramolecular structures. [14, 41] A special case of CAC is a critical micelle concentration (CMC) which is used if the self-assembled structures are micelles.

The CAC has been observed to change with the length of the polymer chain. As its length increases linearly the CAC drops exponentially. [16, 42] The CAC for substances with high molecular weight (M_W), such as polymers, is thus orders of magnitude lower than for small amphiphilic molecules. For example, sodium dodecyl sulphate, with the chain length of mere 12 carbon atoms and a sulphate head group, has CAC $= 8 \cdot 10^{-3}$ mol$\cdot$l^{-1} [43] whereas for polymer chains of approximately 500-600 monomeric units the CAC goes down to the order of 10^{-7} to 10^{-8} mol$\cdot$l^{-1}. [44] This is a significant advantage for biomedical applications of polymer self-assembled systems as it promotes the stability of the particles after they have been diluted by blood following administration into the body. It also means that free unimers have much lower concentration than smaller molecules would have, which is another advantage as these free entities might be undesirable from biomedical viewpoint. [14, 45]

The CAC can be determined by various methods. Some are based on the measurement of abrupt change of physical property, such as surface tension of solution, with polymer concentration, which marks the CAC. Others are based on adsorption of dyes into the assemblies and change in their spectral properties upon their disassembly. [46]

2.1.5 Phase behaviour as a reaction to external stimuli

In some systems of copolymers in solution the change in external conditions can cause phase separation and formation of self-assembled particles. This stimulus can be for example change in temperature, pH or even change in solution composition

such as added salts or solvents. [14] If the triggering external factor is the change of temperature, we call such systems thermoresponsive.

The change of polymer solubility with temperature can be described using the Flory-Huggins theory as discussed above. In the Flory-Huggins approximation only some thermal effects are predicted by the theory however this does not hinder the usefulness of the obtained conclusions. From **Equation 2** we get the experimentally accurate interaction parameter χ. The value of this parameter is based on properties of the system stemming primarily from the polymer monomeric composition and the composition of the solvents. And as by definition this parameter describes the energy cost of interaction between the polymer and solvent. If we consider that the system wants to minimize its free energy the χ value then strongly influences if under specific conditions it is energetically favourable for the system to phase separate or not. Based on this we can view the phase behaviour of the solution using phase diagrams as shown in **Figure 4**. [47, 48]
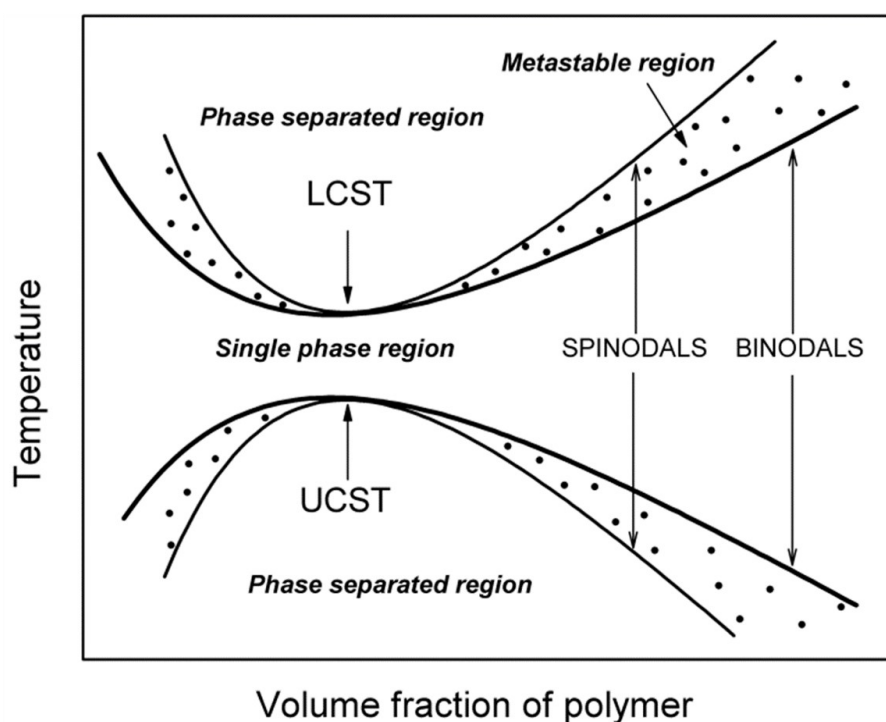

Figure 4 *Schematic example of a phase diagram of thermoresponsive copolymer in solution. Adapted from [49].*

When going from the single phase region to the phase separated region in the phase diagram we can meet the coexistence curve, the binodal, at which the system can be both one phase or two phases depending on nucleation sites and other factors,

if we continue further into the phase separated region we eventually encounter a limit of stability, the spinodal, beyond which the system will always be phase separated into two phases. [47, 48] Between these two curves is the metastable region in which the system can either remain in one phase or separate into two phases. For a certain composition of the solution the binodal and spinodal curves meet at the critical point and define lower or upper critical solution temperature (LCST or UCST). This is descriptive of the polymer behaviour in the solution with varying temperature. That is, for polymer exhibiting LCST behaviour the solution will contain only one phase at temperatures under LCST as the polymer will be always dissolved, while above LCST it may phase separate into polymer rich and polymer poor phase depending on the solution composition. The polymer system with the UCST behaviour exhibits the inverse tendency, meaning it is always in one phase at temperatures above the UCST and can phase separate below the UCST. Interestingly in some cases polymers can even express both LCST and UCST behaviour. [14, 47]

Based on this we can define the cloud point temperature (T_{CP}). This temperature would be specific for the solution composition and it is the temperature at which the amphiphilic molecules begin to aggregate and phase separate from the rest of the solution. The solution usually gains a cloudy appearance in the process meaning its opacity is increased due to the growth of larger particles. [50] In the phase diagram the T_{CP} should lie somewhere between the binodal and spinodal depending on how far into the metastable region the sample gets before phase separating.

For application in biomedical research the polymers exhibiting LCST behaviour in aqueous solutions are far more interesting and focused on as they can be used to formulate smart self-assembled systems reacting to injection from outer colder environment into warmer environment inside the body. [14]

As discussed above the response of polymer systems to external stimuli does not have to be limited to changes in temperature. Changes in pH, additional components and solvents or even light irradiation can be used as well. The response to external stimulus can be used to formulate a copolymer behaving in an advantageous manner. For example, copolymers with hydrophilic and thermoresponsive blocks where the thermoresponsive block is hydrophilic at lower temperatures and becomes hydrophobic at higher temperatures. Such copolymers can self-assemble into particles or depos upon injection into the human body. Copolymers which are responsive to pH

can conversely be built so that they are assembled into particles carrying drugs, as one of their blocks is hydrophobic and the other hydrophilic at normal body pH, but at the site of acidic tumour the hydrophobic block becomes hydrophilic causing disassembly of the particles and deployment of the drug payload in close proximity to the tumour significantly limiting any side effects the drug would have on other parts of the organism. [51, 52]

2.2 Polymer nanoparticles in biomedicine

2.2.1 Application possibilities

Self-assembled polymer nanoparticle systems are increasingly more important as medical materials and prove to have clinical applications in almost all fields of medicine. They are showing great potential in therapeutic as well as diagnostic applications. [53-55]

Many drugs, especially those whose effect is required to be targeted to a specific location in the body, often exhibit some degree of undesirable side-effects. [56] This is typical for example for treatment of cancer. Because cancer cells are derived from healthy cells their molecular targets are present also in healthy cells. Therefore, killing cancer cells by a drug is typically accompanied by some damage to healthy cells and cancerostatics rank among drugs with most significant side effects. [57] The diblock copolymer assemblies, primarily micelles and vesicles, can be used as drug delivery systems to encapsulate bioactive substances and deliver them to target locations for diagnostic or therapeutic effects. [14] Using micelles and polymersomes to encapsulate the drugs allows us to supress their unwanted physicochemical properties, target their biodistribution to certain tissues and under the right conditions even enable a triggered release of the drugs in a specific site. [14] Of course, this specific targeting and active response to changes in environment come hand in hand with increased requirements for greater complexity of the self-assembled systems. [23] Fortunately, the research is now advanced enough that with the right set of parameters even the high complexity, functionalization and targeting can be achieved and formation of complex micelles and assemblies with multiple functions and bioactive properties can be realized. [13, 18]

Even in diagnostics the self-assembled polymer systems can provide significant advantages. In medical practice it is very useful to be able to determine the

precise location of a certain type of tissue, the site of inflammation or a foreign object in the body. The imaging methods such as X-ray, computed tomography (CT) scans or magnetic resonance imaging (MRI) have come a long way since their discovery however their possibilities are still limited in certain ways. To increase their imaging capabilities, contrast agents are often used to help differentiate tissues or objects, at which they accumulate, from the mass of the body. In case of MRI, fluorine-based contrast agents are often used as there is relatively low concentration of fluorine in the human body and they are then well observable. [58-60] Most of the commonly used fluorine contrasts are small-molecules and their usefulness is unfortunately limited by their excessive hydrophobicity and lipophilicity which leads to their poor biodistribution. As discussed above this can be countered by using self-assembled polymer systems which can be tailor made for the required application and targeting of certain tissues. These can then either carry fluorine-based contrast agents loaded inside the assemblies or can contain NMR active fluorine atoms and serve as the contrast agents themselves. [61-63]

2.2.2 Why size matters and the EPR effect

Nanoparticles in the human body have a natural tendency to accumulate in certain organs and tissues such as liver, kidneys, lungs and spleen. Their surface charge, shape and especially their size strongly influence the specifics of this behaviour. The larger they are the higher tendency they show to accumulate in lung capillaries, liver and spleen while the smaller ones around 100-200 nm can be especially interesting as drug delivery systems for treatment of certain cancerous aliments. [64] That is because some types of cancerous tissue grow very fast and their building blocks and structure are not as properly organized as they are in the healthy tissue. The outcome of this is that certain types of solid tumours possess faulty internal vasculature as their new quickly grown veins are fenestrated because their epithelial cells are not in tightly packed contact. [65-67] They also have poor or even completely missing lymphatic drainage, which in healthy tissue should be eliminating any entities too large to be eliminated from the tissue through the blood stream. These two anomalies synergize as the enhanced permeability and retention (EPR) effect and promote accumulation of nanoparticles of up to 200 nm size in such tumour tissues.

This can be exploited to achieve targeted delivery of therapeutic or diagnostic agents into the tumour. [68, 69]

This is also one of the main reasons the self-assembled polymer systems are so interesting for biomedical research. Because many block copolymers can form micelles whose size range is usually from 10 to 100 nm which is ideal for the exploitation of the EPR effect. [70] Their size depends primarily on the length of the polymer blocks and their interactions with each other and the solvent. The size of individual copolymer molecules in solution, represented by their radius of gyration (R_g) is pretty much directly related to their Molecular weight (M_W) or degree of polymerization (N). This can be expressed through relation

$$R_g \sim N^\nu \qquad (4)$$

where ν is the Flory exponent which describes how tightly packed the polymer chain is. [47] The polymer chain in good solvent will be relaxed, highly swollen, forming a loose coil and will have lot of contact area with the solvent molecules. This corresponds to Flory exponent $\nu = \frac{3}{5}$. On the other hand, when the polymer is barely soluble in the solvent and experiences unfavourable interactions with the environment it forms a tightly packed globule to minimize its contact with the solvent molecules. This corresponds to Flory exponent $\nu = \frac{1}{3}$. So, the Flory exponent helps to describe not only the relation between size and degree of polymerization of the polymer but also the interaction of polymer with its environment. As such it can also be used to estimate phase behaviour of copolymers.

2.2.3 Biodegradability of supramolecular systems

As discussed above the polymer assemblies in solution exchange their constituents with their surrounding environment constantly and if they are diluted below the CAC they disassemble into individual unimers. As the nanoparticles circulate, they gradually fall apart meaning that particles measuring tens to hundreds of nanometres in diameter disassemble into unimers of sizes below 10 nanometres. This allows for renal elimination of these unimers from the body as they fall below the threshold for renal filtration. For example, for poly(2-ethyl-2-oxazoline) it is approximately 5 nm. [71-75] This type of physical biodegradability is very

advantageous for drug delivery systems as the particles and polymers are naturally eliminated from the body and do not accumulate in it in any undesirable way.

Another way of elimination of polymer nanoparticles from the body and preventing their accumulation is chemical biodegradability. Some polymers contain chemical bonds which can be cleaved under conditions to which they are naturally exposed inside the body, causing their chains to disintegrate over time. This chemical degradation produces smaller chemical entities which are either biocompatible or harmless and the body usually has built-in mechanisms to eliminate them safely. Polymers exhibiting this chemical biodegradability can be both natural such as starch or gelatin or synthetic such as poly(lactic acid) (PLA) and poly(ε-caprolactone) (PCL). [76, 77]

2.3   Experimental methods

As discussed in section 2.2.2 the size of the polymers and their nanoparticles is an important factor determining their applicability in nanomedicine. It is thus important to determine and control it precisely. This control is achieved through several steps. At the beginning it stems from maintaining consistent properties of the polymers forming the nanoparticles, primarily their composition, length and architecture. [13] It can also depend on the particle forming process as discussed in section 2.1.3.

Consistent properties of the drug delivery systems need to be analysed with high precision to check the dispersity of sizes and properties of the polymers and nanoparticles is minimal. This can be done by a wide array of techniques. Most of them can be categorized between scattering and microscopic methods. [13] We will focus mainly on the scattering techniques as they can observe our samples in solution at biological pressures and temperatures while most microscopic techniques rely on electron microscopy which usually needs dry samples at vacuum or temperatures well below 0°C.

2.3.1 Scattering experiments generally

Scattering techniques are based on interaction of radiation with matter. Generally, four types of result of this interaction are considered as shown in **Figure 5**, reflection, transmission, absorption and scattering.
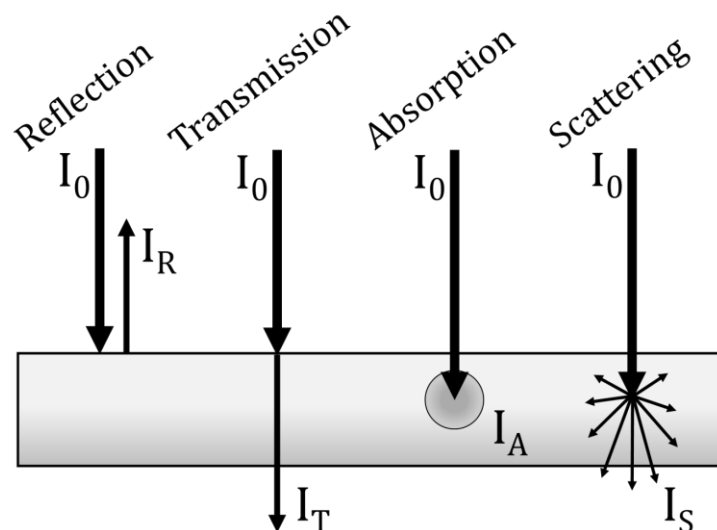
Figure 5 *Four basic types of interaction between radiation and matter: reflection, transmission, absorption and scattering.*

Here we are of course interested in the fourth of these, the scattering. This interaction between radiation and matter can either occur without changing the energy of the radiation, an elastic scattering, or the energy of the radiation is changed in which case the scattering is inelastic. A very important border case is a quasi-elastic scattering in which the energy of the scattered radiation is changed by very small amount when compared to its original energy. This will be further discussed in the dynamic light scattering section 2.3.5 below as it is a phenomenon very frequently utilized in analytical applications of scattering.

The scattering techniques most commonly used for research of polymers and their assemblies are the light, X-ray and neutron scattering. The basic principle is the same for all of these. **Figure 6 (A)** depicts the common arrangement of scattering experiment which can be further improved by multi-dimensional detectors etc. The sample is irradiated by collimated radiation of selected wavelength. This primary radiation interacts with the sample based on the properties of the radiation and the sample, which are different for each type mentioned above, and then the radiation scattered from the original direction of the primary beam is measured. The relation of the incident and scattered wavevectors ($\vec{k_I}$ and $\vec{k_S}$, respectively) can be depicted as seen in **Figure 6 (B)**.
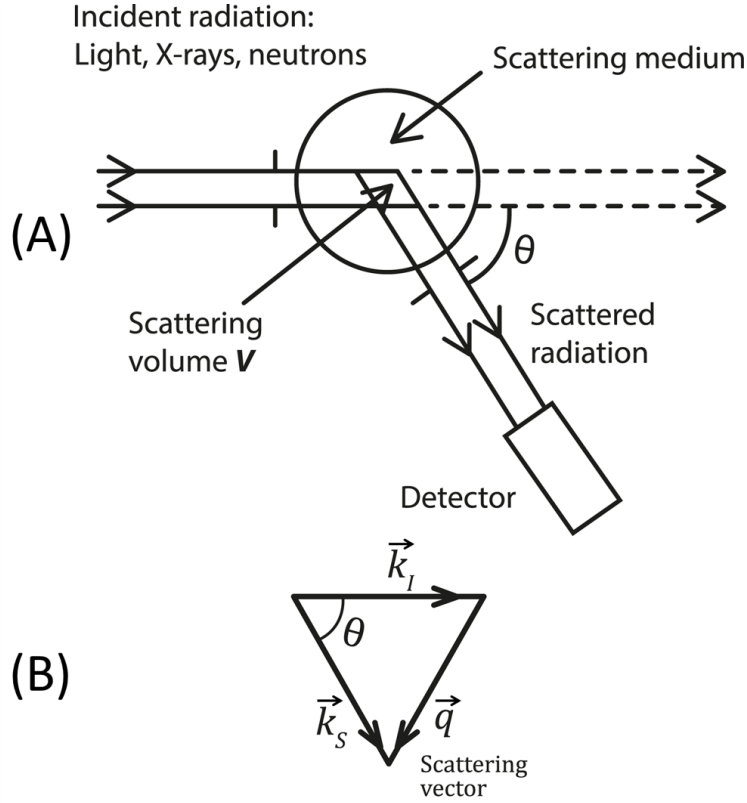
Figure 6 *Scheme of general scattering experiment setup (A) and geometrical scattering vector definition (B). Adapted from [78].*

From this relation we can define scattering vector $\vec{q}$ as a difference between wavevectors of the incident $\vec{k_I}$ and scattered $\vec{k_S}$ radiation.

$$\vec{q} = \vec{k_S} - \vec{k_I} \tag{5}.$$

For elastic scattering we can say that wavelength of scattered radiation is unchanged and so from the geometry depicted in **Figure 6 (B)** we get

$$q = \frac{4\pi}{\lambda} \sin\left(\frac{\theta}{2}\right) \tag{6}$$

where λ is the wavelength of radiation in the matter and θ is the scattering angle.

There are two basic measurement modes that are applied for scattering experiments. The first is the static scattering which measures the average intensity of the scattered radiation at various angles. By analysing this scattering pattern, we can obtain information on the size, shape, internal structure. If appropriate calibration of the instrument is carried out it can even provide the molar weight of present particles. The second mode is the dynamic scattering which measures the intensity of scattered radiation at a certain angle or angles as a function of time. This gives us information

on the dynamics of the sample. From this measurement we can obtain information on apparent size and possibly structure if coupled with the static scattering. [79, 80] It is worth noting, that scattering techniques analyse vast numbers of particles at the same time and as such provide excellent statistics of the sample.

The measured intensity of scattered radiation $I(q)$ can be generally described by following relation [47, 79, 81-83]

$$I(q) \sim I_0 \frac{1}{\lambda^4} \frac{1}{r^2} Q_E \, M \frac{N}{V} (\rho_1 - \rho_2)^2 F(q) S(q) \qquad (7).$$

The first part (in blue colour) represents the instrumental parameters, where I_0 is the incident intensity at the sample, r is the distance between sample and detector and Q_E is detector sensitivity. The second part represents the material parameters, where M is the molar mass of the scattering objects, N is the number of objects in the scattering volume V irradiated by the incident beam and the ratio $\frac{N}{V}$ represents the concentration of the scatterers in the sample, ρ_1 and ρ_2 are properties of the scattering object and environment respectively and their difference $(\rho_1 - \rho_2)$ is the scattering contrast, $F(q)$ represents the form factor of the object which includes its size and shape, and $S(q)$ represents the structure factor, which describes the arrangement of the scatterers with relation to one another inside the sample. Some of these terms might be neglected under appropriate conditions such as neglecting structure factor in sufficiently dilute samples.

As described by the scattering contrast term in **Equation 7**, scattering does not occur in perfect crystals and by extension scattering does not occur in pure unperturbed solvents we consider in this idealized situation. [47] So, radiation is scattered only when there are some heterogeneities in the material. These heterogeneities can be for example polymer molecules or self-assembled nanoparticles. Of course, their properties must be different in some manner from properties of the surrounding solvent the provide non-zero contrast term. Each type of radiation interacts with the matter in somewhat different manner and so the physical properties acting as contrast for their scattering are also different. We list these properties for the three discussed types of radiation in **Table 1**. [84]

Radiation		Light	X-ray	Neutron
Contrast factor	Name	Refractive index increment	Electron density	Scattering length density
	Symbol	$\dfrac{\partial n}{\partial c}$	ρ_e	SLD

Table 1 *Scattering contrast properties for light, X-rays and neutrons.*

2.3.2 Static light scattering

If the incident radiation is the electromagnetic radiation with wavelengths within or close to visible light, we speak of static light scattering (SLS). The heterogeneity causing the scattering is the difference between the refractive index of solvent and particle, which basically represents the difference in their polarizability by the light radiation. [47, 48, 84] The contrast factor is then the change in the refractive index as a function of concentration.

We consider the case of light polarized perpendicularly to the observation plane as that is the most common experimental setup for light scattering experiments and is easily realizable. The simplest situation of light scattering experiment for our applications is the scattering of dilute polymer solutions. Under the assumption that the polymers are sufficiently small and the solution sufficiently dilute we consider that we are only interested in light scattered by the polymers. This means light scattered by the solution in excess of light scattered by the pure solvent. Thus, we obtain equation

$$\frac{I_{ex}}{I_0} = \frac{4\pi^2 n^2 (\partial n/\partial c)^2}{r^2 \lambda_0^4 N_{av}} \frac{c}{\left(\frac{1}{M_W} + 2Bc + \cdots\right)} \tag{8}$$

where I_{ex} is the intensity of light scattered just by the polymers in excees of the light scattered by the pure solvent, I_0 is the intensity of the incident radiation, n is the refractive index of the solution, $\frac{\partial n}{\partial c}$ is the refractive index increment for the solution and polymer, r is the distance from the scattering object, λ_0 is the wavelength of the incident light, N_{av} is the Avogadro's number, c is the concentration of polymer in the solution, M_W is the molar weight of the polymer chains and B is the second virial coefficient. The refractive index increment $\frac{\partial n}{\partial c}$ is the contrast of polymer for the incident light and can be measured directly by differential refractometry or it can be found in tables. The second virial coefficient B describes the interaction between

individual polymer chains and if they are more attractive or repulsive when compared to interactions with the solvent.

To simplify **Equation 8**, we define a few new terms.

$$R_\theta = \frac{I_{ex} r^2}{I_0} \tag{9}$$

defines the Rayleigh ratio, which describes how much light is scattered in proportion to the intensity of the incident light. We also define

$$K = \frac{4\pi^2 n^2 (\partial n/\partial c)^2}{\lambda_0^4 N_{av}} \tag{10}.$$

Equations 9 and **10** allow us to simplify the format of the **Equation 8** to

$$\frac{Kc}{R_\theta} = \frac{1}{M_W} + 2Bc + \cdots \tag{11}.$$

This equation describes Rayleigh scattering of dilute polymer solutions. Rayleigh scattering is usually used as a model applicable for dilute solutions of particles whose size meets the requirement that $qR_g \ll 1$. For macromolecules this generally means $R_g < 5$ nm which should typically correspond to molar weights below 10^5 g·mol^{-1}. This size limit depends on the wavelength of the scattered light so this estimate is made for $\lambda_0 \approx 500 \, nm$. Put simply the Rayleigh scattering is valid only for particles whose size is much smaller than the wavelength of incident radiation. For such small scatterers we can assume, that their scattering is incoherent, meaning their scattering is not systematically dependent on one another as there is no connection between them and there are no significant interference effects that would change the resulting scattering pattern. [47]

If the size of the particles in the solution rises so that our assumption of small size no longer applies, but we still maintain sufficient dilution so that positions of individual particles are not correlated in any way, we also need to consider the effects of interference of light scattered from different parts of the same particle. We define a form factor $F(\theta)$ as a ratio between the light actually scattered by the sample and the light expected to be scattered by Rayleigh relation for scattering (**Equations 8** and **11**)

$$F(\theta) = \frac{I_{Actual}(\theta)}{I_{Rayleigh}(\theta)} \tag{12}.$$

As a note if we considered that our dilution assumption is not valid as well, we would also be defining a structure factor $S(\theta)$ however that is not necessary for dilute solutions that are usually investigated for biomedical applications.

This universally defined form factor is dependent on the specific sizes and shapes of particles present in the sample. However, if we restrict ourselves on isotropic samples meaning that the imagined vectors between individual small parts in the particles have no preferred orientation in the sample, we obtain

$$F(q) = 1 - \frac{1}{3}q^2 R_g^2 + \cdots \tag{13}$$

where q is the scattering vector and R_g is the radius of gyration of the particle. This form factor is applicable for experiments in which $qR_g \rightarrow 0$. From **Equation 13** it can be seen that this $F(q)$ is independent of shape of the particle and so if we design our experiments to satisfy the requirement above either by measuring only small particles or by appropriate choice of wavelength and measurement angles, we can calculate the radius of gyration of our particles R_g from scattering experiments.

Now if we combine the obtained form factor from **Equation 13** and the Rayleigh scattering from **Equation 11** we uncover the cornerstone equation for static light scattering of dilute polymer solutions which is the Zimm equation

$$\frac{Kc}{R_\theta} = \frac{1}{M_W} + \frac{q^2 R_g^2}{3M_W} + 2Bc + \cdots \tag{14}.$$

Based on this equation we can carry out a set of measurements on samples with various concentrations and at various angles and from this experiment we can extrapolate the molar weight and the radius of gyration of the polymers or particles and the second virial coefficient. This measurement can be processed into a Zimm plot which is depicted in **Figure 7**. From the acquired data we can perform projection of intensities at given angles and concentrations to zero scattering angle and zero concentration. The slope of the angular dependence extrapolated to zero concentration gives us size of the particles R_g and the slope of concentration dependence extrapolated to zero angle gives us the second viral coefficient B. The intersect of the projected dependencies with the $\frac{Kc}{R_\theta}$ axis will give us the molar weight of the measured particles $\frac{1}{M_W}$.
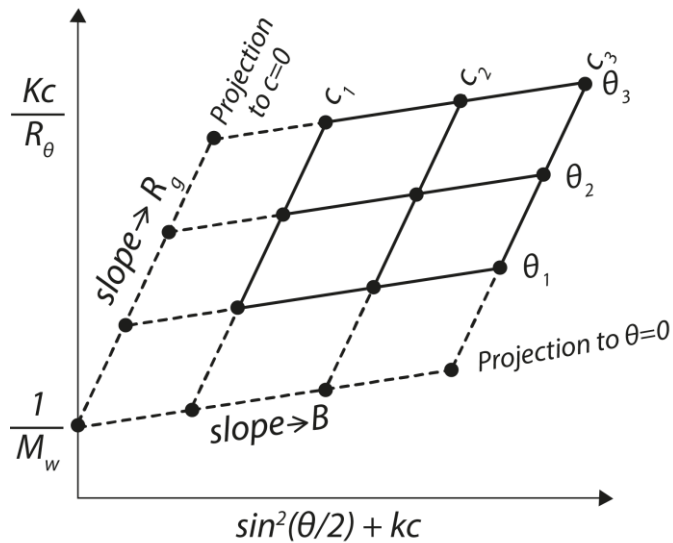
Figure 7 An example of the Zimm plot with data and projection to zero angle and concentration. Adapted from [85].

2.3.3 Small angle X-ray scattering

We can also attempt to scatter electromagnetic radiation of much shorter wavelength such as X-rays whose energies are much higher. For polymers and their self-assembled structures the small angle X-ray scattering is usually used. Due to shorter wavelength X-ray interaction with matter occurs on different scale than visible light, meaning that X-rays are scattered by electrons of atoms, [79] and so the contrast factor is different from visible light. For X-rays the contrast is the electron density which increases with the atomic number of the given element. This means that heavier atoms will scatter more than lighter ones which can be used with advantage to enhance X-ray scattering of certain parts of the investigated particles if heavier elements are present in those parts. This can be achieved for example by addition of heavy counterions which adsorb to particle surface. [79, 80]

The much shorter wavelength of the X-ray radiation also causes that the values of scattering vector q can be much higher than for visible light and thus we are probing much smaller dimensions, meaning either smaller particles or even their internal structure. [79, 80]

2.3.4 Small angle neutron scattering

Somewhat analogously to SAXS we can also scatter neutron radiation on polymer samples in the small angle neutron scattering experiments.

25

The nature of this radiation is very different from electromagnetic waves. As neutrons do not carry any charge and are rather heavy, at least among the particular atomic constituents, they interact directly with the atom core via the strong interaction. The contrast factor for them is thus the nuclear scattering length density (SLD) which is characteristic for each atom and as such SLD of any material needs to be calculated from its chemical composition and density. [79, 80]

It is very interesting to note that the SLD for hydrogen is -3.74 fm while SLD for deuterium is 6.67 fm. [86, 87] This major difference allows the use of the index matching technique, which is analogous to index matching in optics. As mentioned above the scattering occurs only if there are any disturbances or contrast in the scattering medium. For index matching experiment we consider a particle that contains sections with different SLDs, for example a hydrophobic core and a hydrophilic corona of a micelle. A mixture of deuterated and normal solvents in an appropriate ratio can then have the same SLD as one of the particle sections. This effectively makes the section invisible for the incident neutrons and only the sections of the particle whose SLD is different from the rest of the sample can scatter any neutrons and be detected. If successful this method is exceptionally useful for uncovering internal structures of particles which would otherwise remain hidden. [80]

2.3.5 Dynamic light scattering

One of the most commonly used techniques for analysis of size distribution of particles in solution is the dynamic light scattering. In the static scattering experiments changes in total scattered intensity with different scattering angles were investigated. Conversely in the dynamic scattering experiments the changes of scattered intensity in time at one angle are measured. [80, 88, 89]

The dynamic light scattering experiments are based on quasi-elastic scattering of photons on particles moving in the solution. The particles are in constant Brownian motion and thus the wavelength of light scattered by them is affected by the Doppler effect, causing widening of the spectral line by a very small amount as the change in energy of the scattered photons is miniscule when compared to the original energy of the incident photons. With modern techniques it is possible to measure this shift, however it is highly impractical and for decades now other techniques have been employed to investigate this phenomenon. [90-92] Instead of attempting to measure

26

the change in wavelength of the scattered light wave we turn to measuring the changes of its intensity throughout the time $I(t)$. From this we obtain the intensity auto-correlation function as defined in **Equation 15** and shown in **Figure 8**.

$$G_2(t) = \frac{< I(\bar{t})I(\bar{t} + t) >}{< I(\bar{t}) >^2} \tag{15}.$$

The angled brackets represent averaging over time. From $G_2(t)$ we learn how quickly the measured intensity stops resembling itself. That is if we compare intensities in times $\bar{t}$ and $\bar{t} + t$ it provides the measure of how fast they become random and completely unrelated to one another.
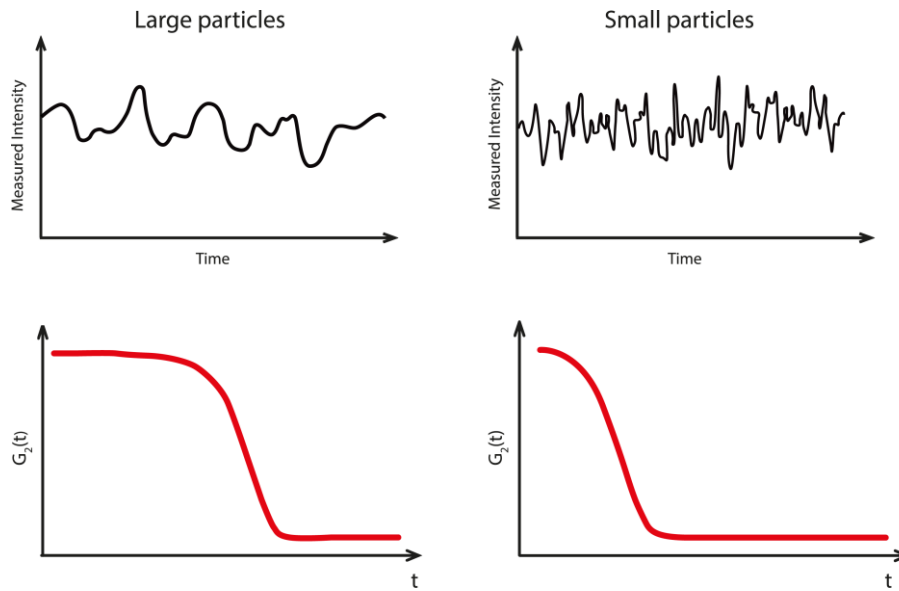

Figure 8 *Imagined measured intensities for large and small particles and their transformation into corresponding correlation curves.*

The intensity auto-correlation function $G_2(t)$ is what is primarily obtained from an experiment. However, it is not possible to determine the absolute movement of particles from the fluctuations of the measured intensity. These fluctuations are caused by relative movement of the particles with relation to one another. The light scattered by individual particles interferes together and creates a speckle pattern in the observed space. As the particles move, this speckle pattern changes and the total detected intensity fluctuates as the interference conditions change with relative positions of the moving particles. This leads us to the electric field correlation function $G_1(t)$, which is connected to the relative movement of particles and is defined by relation

$$G_1(t) = \frac{<E(\bar{t})E(\bar{t}+t)>}{<E(\bar{t})>^2} \qquad (16).$$

Through the standard relation between intensity and electric field of light $I \approx |E^2|$ we can then express the intensity auto-correlation function through the Siegert relation as

$$G_2(t) = Z[1 + \beta|G_1(t)|^2] \qquad (17)$$

where Z and β are constants describing the baseline and instrumental response respectively.

So, to summarise, the intensity correlation function $G_2(t)$ describes the rate of changes in the measured scattering intensity. The electric field correlation function $G_1(t)$ determins how the movement of the particles in the sample is correlated and the Siegert relation connects these two relating the measured physical quantity (intensity of scattered light) to what is actually happening in the sample (the speed of the particle motion). We can finally express the electric field correlation function from the Siegert relation as a function of the intensity auto-correlation function $G_2(t)$ through a relation

$$G_1(t) = \sqrt{\frac{\frac{G_2(t)}{Z} - 1}{\beta}} \qquad (18).$$

This then provides the basis for evaluation of the measured data. The movement causing the discussed decay of correlation in $G_2(t)$ is the Brownian motion of the particles. The rate of this motion can be related to their size by the Stokes-Einstein equation for Brownian motion

$$D = \frac{k_B T}{6\pi\eta R_h} \qquad (19)$$

where D is the diffusivity, k_B is the Boltzman constant, η is the viscosity of the sample, and R_h is the hydrodynamic radius of the particles.

For a sample of uniform particles, the electric field correlation function can be considered as a monoexponential decay

$$G_1(t) = \exp(-\Gamma t) \qquad (20)$$

where Γ is the decay constant which is the inverse value of the relaxation time τ.

$$\Gamma = \frac{1}{\tau} \qquad (21).$$

The decay constant of the electric field correlation function and the diffusivity are related through equation

$$\Gamma = Dq^2 \tag{22}$$

where q is the value of the standard scattering vector as defined in **Equation 6**. [89]

Thus, by linking all these together it is possible to obtain the hydrodynamic radius of the particles in a sample from measuring the intensity of the scattered light as a function of time.

$$R_H = \frac{k_B T q^2}{6\pi\eta}\tau \tag{23}.$$

Of course, real polymer samples almost never contain only a single population of perfectly uniform particles, the rare exception being for example some pure proteins, but instead particles of various sizes are present in the samples. These are usually described by particle size distribution function. From measuring real samples, we thus get a multiexponential decay of correlation and the electric field correlation function $G_1(t)$ becomes more complicated. This can be generally expressed as a relation

$$G_1(t) = \int A(\tau)\exp\left(-\frac{t}{\tau}\right)d\tau \tag{24}$$

where $A(\tau)$ is the distribution of relaxation times τ. When uncovered, $A(\tau)$ allows the calculation of distribution of sizes of particles present in the sample. There are several methods used for calculation of $A(\tau)$ from the measured multiexponential decay. Probably the most widely used is the constrained regularization method for inverting data (CONTIN) which uses the inverse Laplace transformation of the $G_1(t)$ to obtain the $A(\tau)$. In CONTIN, same as in other algorithmic methods, it is necessary to stop the analysis of the data at some point by an appropriate choice of limiting factors so that the model does not try to analyse meaningless information of noise etc. Based on the set limitations CONTIN chooses distribution function with the least detailed distribution that agrees with the data to a prescribed degree. [90-93] The choice of these limits also determines how different two particle populations need to be to be distinguished by the analysis and not considered as a part of the same wider population. [13]

It is very important to note that the obtained hydrodynamic radius for a particular particle is the radius of a hard sphere which would have the same diffusion

coefficient as the measured particle. So, the hydrodynamic radius is usually not the same as the actual size of the particle nor is it usually equal to the radius of gyration which could be obtained from the static light scattering. Even so for polymer samples it is the most used descriptor as the dynamic light scattering measurements allow for consistent comparison among large number of samples with much simpler and thus cheaper instrumentation.

The size distribution obtained from the DLS experiment is an intensity-weighted size distribution or simply intensity distribution. Meaning that the distribution is weighed according to the amount of light scattered by individual particles of a given size. However, in many papers the volume or number-weighted size distributions are preferred. This however can lead to introducing a significant error as for a precise recalculation from the intensity to volume or number distribution the from factor of the particle has to be known. In most cases however these recalculations are made based on an assumption that the measured particles are hard spheres whose scattered light intensity is proportional to the third power of their size $I \approx R^3$. It is of course true that larger particles scatter significantly more light than smaller particles and as such are much more prominent in the intensity distribution, as is graphically illustrated in **Figure 9**, however basing recalculation of various nanoparticles with different shapes and structures purely on hard sphere form factor can significantly change the final result. [80]

Because the range of investigated sizes covers several orders of magnitude the calculated size distributions are typically plotted against a logarithmic axis of hydrodynamic size. This has the unfortunate effect causing that two particle populations which would scatter the same amount of light seem disproportionate in the graph even though the area under their corresponding peaks is technically the same. This can and in practice generally is mitigated by equal-area representation in which the data is plotted not as the distribution function of sizes $A(R_h)$ but as a product $R_h A(R_h)$. This way the two equally scattering populations are shown in the graph as visually equivalent. All our DLS data are presented in this format and as customary the vertical axes are marked Intensity. [89]
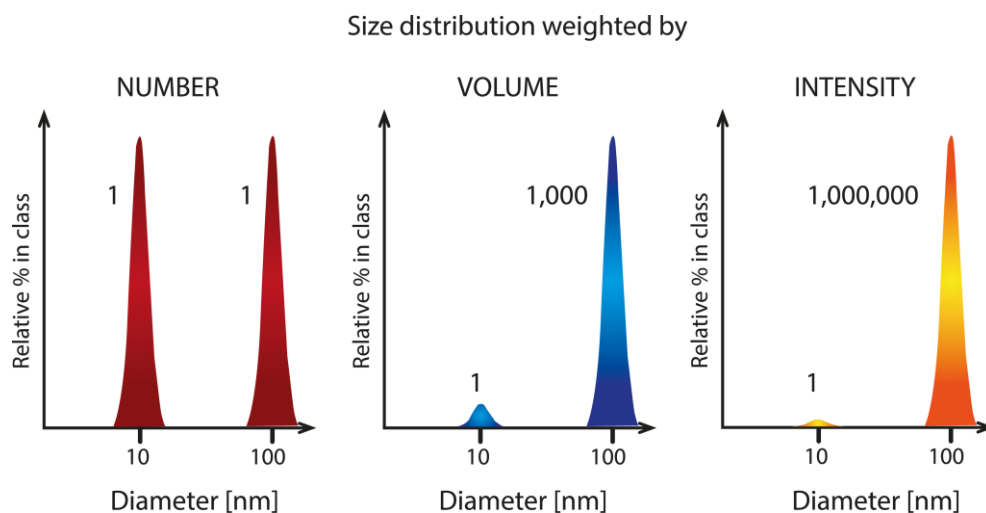
Size distribution weighted by

| NUMBER | VOLUME | INTENSITY |

Figure 9 *Example of graphical comparison of number, volume and intensity distributions of a mixture of two populations of particles with sizes 10 nm and 100 nm present in equal numbers in the sample. Adapted from [94].*

The discussed theory also provides some considerations which should be kept in mind when performing scattering experiments.

From the mentioned steep dependence of scattered intensity on size of particles it should be clear that it is very important to keep all samples for scattering experiments as clean as possible, especially dust free. This is usually ensured by filtering all samples prior to measurement and keeping them in cleaned and sealed containers. This is of course possible only if filtering the sample does not change it.

Another concern pertaining to both the DLS and SLS measurements is that samples have to be dilute enough that multiple scattering does not occur. Multiple scattering is a phenomenon during which a photon which was already scattered once is scattered again before reaching the detector. Thus, if there are too many scatterers in the sample, multiple scattering introduces experimental errors into the results.

As discussed above, the intensity fluctuations measured during the DLS experiments are assumed to originate from the random Brownian motion of the particles. If other sources of movement are present the measurement detects them as well and they also introduce some form of error. Among these additional sources of unwanted movement are sedimentation, in case the particles are too big and dense, thermal currents caused by the temperature differences inside the sample volume, and others. Because of this the DLS experiment intended to measure the R_h has to be designed in a manner which mitigates these other types of movement.

Curiously enough one of these other types of movement can be used to probe different characteristics of the particles, namely their surface zeta-potential. If electric current is applied to the sample the particles will move to the electrodes based on their charge. If the current and other factors are known it is then possible to determine the zetapotential of the particles from this specialized DLS measurement.

2.3.6 Nuclear magnetic resonance spectroscopy

Nuclear magnetic resonance (NMR) spectroscopy is a non-destructive analytical technique based on the interaction between magnetic fields and nuclear magnetic moments $\vec{\mu}$ of atoms. The magnetic moment of an atom stems from the spin of its protons and neutrons. Any nucleus with non-zero total spin has a magnetic moment and thus can be detected through NMR. This is routinely used for organic compounds which generally contain significant number of hydrogen ^{1}H or carbon ^{13}C atoms, which are the most commonly investigated atoms in the NMR spectroscopy.

In the basic NMR spectroscopy experiment the nuclear magnetic moments of the atoms in the investigated molecule are first aligned by strong external magnetic field $\vec{B_0}$, around which they start to precess at specific Larmor frequency. The Larmor frequency depends on strength of the static magnetic field and on the type of isotope so at given $\vec{B_0}$ this frequency is characteristic for different isotopes. The aligned magnetic moments are then deviated from their positions by an electromagnetic pulse with frequency similar to that of Larmor frequency of the nuclei. After this excitation pulse is finished, the deviated magnetic moments start to return to the alignment dictated by the static field $\vec{B_0}$. This process can be detected as an induced electric current in a detection coil. The measured current has a sinusoidal evolution with exponentially decreasing amplitude. This measured free induction decay (FID) of the current can then be inverted through a Fourier transform into a frequency spectrum which contains the precession frequencies of the present nuclei.

If all the nuclei were under identical conditions, then all would exhibit the same FID signal. However, in reality the individual atoms inside the molecule are usually in different chemical environments. This influences the electron density of the studied atom and through electron shielding influences the effective magnetic field the nucleus of the atom is exposed to. This causes, that different nuclei provide slightly different

signals. Analysis of the differences in the signals of individual nuclei provides basic information on the internal structure of the investigated molecule.

It is possible to design specialized experiments utilizing complex pulse sequences of the oscillating magnetic field which allow us to uncover additional information about the samples. Various methodologies were developed such as diffusion ordered spectroscopy (DOSY) or the nuclear Overhauser effect spectroscopy (NOESY).

The DOSY experiments separate signals of different nuclei based on the diffusion properties they experience inside the sample, meaning they provide information on how either different molecules or individual parts of the molecules move. This is achieved by applying a pulsed field gradient which momentarily causes the nuclei at different positions in the sample to feel different magnetic field effectively altering their Larmor frequency in spatially defined manner. This way the individual nuclei are labelled according to their position in the sample and it is possible to trace how much they have moved over a period of time.

The NOESY experiments help to determine the spatial proximity of two nuclei whose interaction is not mediated *via* chemical bonds. This provides us with information on the geometry of molecules or possible weak interactions requiring close contact of certain groups. This close proximity determination is achieved through nuclear Overhauser effect during which the nuclear spin polarization of a stimulated population of nuclei (the source nuclei) is transferred to another (the nuclei of interest). The transfer can occur only between nuclei that are no more than 4-6 Å apart.

This description of DOSY and NOESY is very simplified. Full description of the methods can be found for example in [95].

Another technique based on NMR and widely used in medicine is the magnetic resonance imaging which is capable of providing an image of different tissues inside the body. [96] MRI instruments in general medical practice are tuned for ^{1}H hydrogen signal detection. Because fluorine atoms ^{19}F have gyromagnetic ratios very close to those of ^{1}H atoms, they can also be detected by existing ^{1}H MRI instruments with minor adjustments. Moreover, ^{19}F atom is almost as sensitive in NMR as ^{1}H. This makes ^{19}F atoms prime candidates for development of contrast agents for MRI. [58-60, 97]

3 Results

The research discussed in this thesis had several aims:

- Analysis of newly designed fluorinated thermoresponsive block copolymers and primary assessment of their self-assembly properties.
- In depth analysis of samples chosen from the whole set of fluorinated copolymers for their biomedical application prospects.
- Large-scale comparison between block and gradient copolymers and their particle-forming properties in regard to biomedical applications.

These aims were realized and the results published in four articles this thesis is based on. These articles are enclosed to this thesis as Attachments 1-4. The research covered in these articles corresponds to the multidisciplinary field of biomedicine, stretching from polymer chemistry to synthesize the polymers, through physical analysis covering several highly specialized experimental techniques for characterization of the samples, to biological methods testing the practical applicability of the polymer systems in biomedical use.

The author of this thesis focused primarily on the physical analysis and measured all the data from DLS, SLS and SANS methods, processed and evaluated all the data from DLS and SLS, participated on processing and evaluation of the data from SAXS and SANS experiments, and contributed to interpretation of the NMR data in context of all the results obtained for the polymer nanoparticles.

3.1 Primary assessment of self-assembled thermoresponsive copolymer systems for ^{19}F MRI

3.1.1 Polymer description

In the first phase of the research, we analysed two sets of thermoresponsive block copolymers prepared by my colleague, Kristýna Kolouchová, at the institute. These copolymers were designed to have a hydrophilic and thermoresponsive blocks so that they would self-assemble above certain temperature. The hydrophilic block was prepared as a biocompatible copolymer, either poly[*N*-(2-hydroxypropyl) methacrylamide] (PHPMA) or poly(2-methyl-2-oxazoline) (PMeOx), to shield the

core of the particle from undesirable biological interactions after self-assembly. The thermoresponsive block was designed to contain large amounts of fluorine atoms suitable for detection in ^{19}F MRI. For this purpose the poly[N-(2,2-difluoroethyl)acrylamide] (PDFEA) has been selected. This gives us the PHPMA-*block*-PDFEA and PMeOx-*block*-PDFEA copolymers. Three versions of each were prepared differentiated by varying ratio of lengths of their hydrophilic and thermoresponsive blocks. Their code designation, molar weights and their dispersity are listed in **Table 2**.

Polymer	Code	Block ratios	M_W [kg·mol^{-1}]	Đ	T_{CP} [°C]	R_h [nm]
PHPMA-*block*-PDFEA	HF1	2:1	17.5	1.10	37	123
	HF2	1:1	33.7	1.06	31	35
	HF3	1:2	51.5	1.07	23	77
PMeOx-*block*-PDFEA	MF1	2:1	12.7	1.07	31	670
	MF2	1:1	16.2	1.06	30	31
	MF3	1:2	24.5	1.08	33	47

Table 2 *Characteristics of the investigated diblock copolymers and their self-assembled systems. Block ratios as determined by NMR spectroscopy, molar weight of the polymer molecules (M_W) and its dispersity (Đ) as determined by SEC. Cloud point temperature (T_{CP}) and hydrodynamic radius (R_h) of the most prevalent particle population at 37°C as measured by DLS. Adapted from [98].*

3.1.2 Analysis of self-assembly by scattering and microscopic methods

We investigated the self-assembly behaviour of all the copolymer samples in the aqueous environment by dynamic light scattering experiments using the Zetasizer NanoZS instrument (Malvern Instruments, UK). Samples were prepared as 1 mg·ml^{-1} solutions in milli-Q water, cooled in fridge and filtered through 0.22 μm syringe filters prior to measurement. We measured the intensity size distributions of hydrodynamic radii of particles present in the sample at a range of temperatures from 10 to 50°C. The obtained data were processed into multi-dimensional graphs where the changes in size distributions can be observed with changing temperature. These are presented in **Figure 10**.
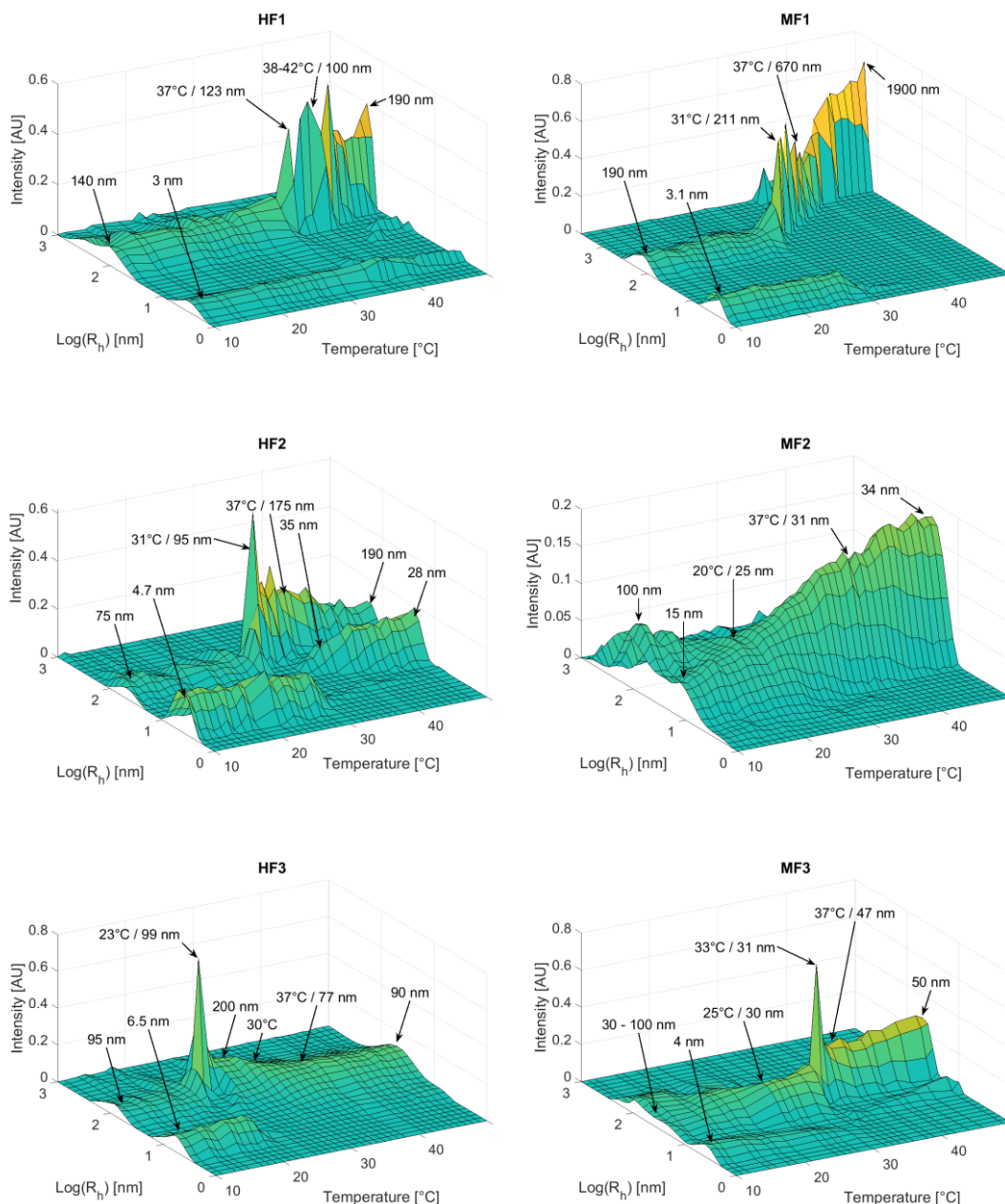
Figure 10 *The thermal dependence of the intensity-weighted size distributions of self-assembled copolymer systems of diblock copolymers PHPMA-block-PDFEA and PMeOx-block-PDFEA (HF1-3, MF1-3). [98]*

For all investigated copolymers temperature-dependent behaviour in solution has been detected. At temperatures above the cloud point temperature (T_{CP}) characteristic for individual samples as listed in **Table 2**, the individually dissolved copolymer molecules began to assemble to form larger particles. For the samples containing PHPMA the T_{CP} was strongly dependent on the ratio of lengths of the hydrophilic and thermoresponsive blocks. The samples with PMeOx hydrophilic

blocks have not exhibited this trend. A higher overall content of a thermoresponsive block in a copolymer should result in a lower T_{CP}, however this effect seems to depend on the type of hydrophilic monomer as well. Similar behaviour has been previously described for other systems. [99]

The change of T_{CP} with concentration has been studied. The concentration had only marginal influence on the T_{CP} as even samples with 10 times lower concentration showed no significant shift of T_{CP}. This finding is important for practical bio-applications in which the sample would be diluted by body fluids.

A study was performed to establish if the thermally induced self-assembly of copolymers was reversible. After reaching the temperature of 50°C at which it has been confirmed the thermal changes occurred the sample was cooled directly to 10°C and a series of measurements of the size distributions was performed. As the samples were cooled below the T_{CP} the observed particles disassembled rapidly into single molecules and the observed self-assembly was found to be reversible. This experiment served to show that the obtained nanoparticles do not form crystalized structures after self-assembly in water or otherwise resist spontaneous disassembly as that would hinder their biodegradability as discussed in section 2.2.3.

The results of the DLS measurements show that below the T_{CP} two particle populations are present in the samples, with the exception of copolymer MF2. Smaller entities ($R_h \sim 3 - 7 \, nm$) should correspond to free individually dissolved polymer molecules in solution. The larger entities correspond to particles that are always present even at lower temperatures resulting from the partial aggregation between copolymers. It is important to note that since larger particles scatter much more light than smaller particles, the larger particles are present in negligible quantity when compared with the unimer population.

When the sample reached the T_{CP}, the observed unimer population quickly disappeared and a population of larger nanoparticles arose as the unimers self-assembled. In our experiments this was accompanied by an abnormal increase in the intensity of scattered light which corresponds to the anomalous micellization. This phenomenon occurs in some thermoresponsive block copolymers and its suspected source are trace amounts of homopolymer remaining in the sample from synthesis. [100] So, it would seem even though our synthesized copolymers have very low polydispersity indicating high quality of preparation, some trace amounts of free

homopolymers were still present in the samples. The values of measured R_h of the most prevalent particles of the copolymers at 37 °C are listed in **Table 2**.

For both studied types of copolymers (PMeOx-*block*-PDFEA and PHPMA-*block*-PDFEA) the samples with ratio of hydrophilic : thermoresponsive block 2:1 (MF1 and HF1) formed larger particles while samples with ratio 1:2 (MF3 and HF3) formed smaller particles. Based on these results the copolymers MF3 and HF3 with the highest content of thermoresponsive block were selected as the best prospective candidates for bio-applications as they formed nanoparticles in a size range that is well suited for imaging of tumours due to the EPR effect as discussed in section 2.2.2.

These two samples were further analysed by static light scattering. These experiments helped to determine the molecular weights (M_W), radii of gyration (R_g), and densities (ρ) of the nanoparticles formed by these copolymers at 37 °C. The calculated results are presented in **Table 3**.

Sample code	$M_W \cdot 10^6$ [g·mol^{-1}]	R_g [nm]	ρ [g·cm^{-3}]
HF3	66.8	106	0.022
MF3	10.4	67	0.013

Table 3 *The molecular weights (M_W), radii of gyration (R_g), and densities (ρ) of the nanoparticles formed by copolymers HF3 and MF3 at 37 °C as measured by SLS. Adapted from [98].*

Transmission electron microscopy (TEM) was performed with a microscope Tecnai G2 Spirit Twin 12 (FEI company; Czech Republic). An example of obtained TEM images is shown in **Figure 11**. Particles seen in TEM image for MF3 exhibited overall lower average size than particles seen in HF3 which is in perfect agreement with the light scattering experiments.
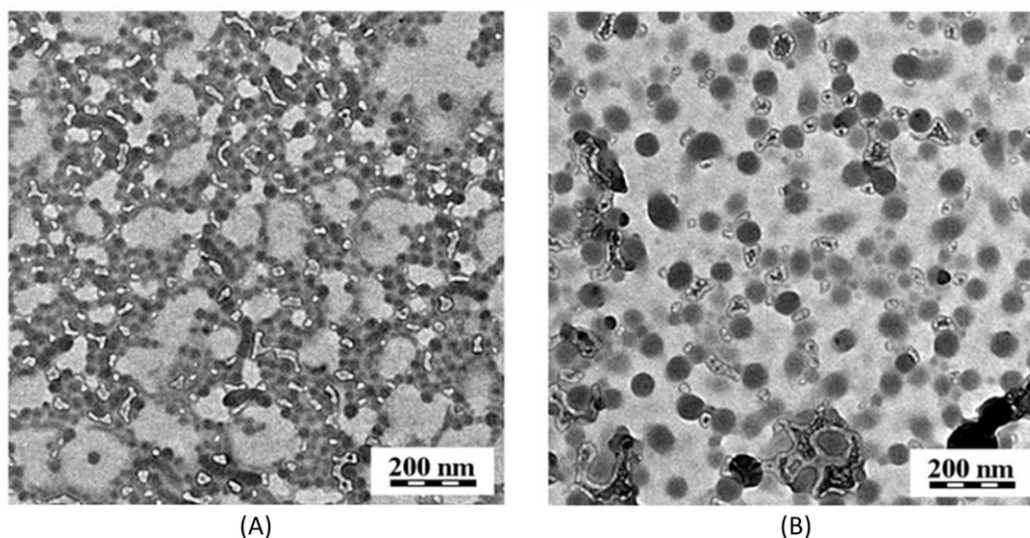
Figure 11 *TEM micrographs of particles self-assembled from (A) PMeOx-block-PDFEA (1:2, MF3) and (B) PHPMA-block-PDFEA (1:2, HF3). Adapted from [98].*

The combination of results obtained from the DLS, SLS and TEM images suggests that the investigated copolymer samples self-assemble into a nanogel. This is based on several observations we discuss further and from these we attempted to form a hypothesis regarding the specific internal structure of the observed nanoparticles.

The investigated nanoparticles are too large to be micelles and their overall calculated density was very low. The molecular weight of even the smaller self-assembled particles as calculated from SLS indicates that approximately 500−1000 polymer chains form one nanoparticle, whereas a micelle usually contains approximately 10−100 polymer chains. This would suggest that these particles could be either vesicles or nanogels. From the TEM images it can be seen that the distribution of mass in the particles seems to be homogenous and not concentrated in the shells of the particles which would otherwise be typical for a vesicle.

The size ratio between thermoresponsive and hydrophilic blocks of amphiphilic block copolymers has generally a significant influence on the morphology of nanoparticles formed by their self-assembly in aqueous solutions. In particles of block copolymers with high degree of internal organization, such as micelles and vesicles, it is usually observed that the polymers with smaller hydrophobic blocks form smaller micelles whereas polymers with larger hydrophobic blocks form larger particles, as shown in [101]. This is in direct contrast with behaviour of our particles leading us to believe their internal structure shows only lesser degree of organization. As such these results seem to be indicative of a nanogel internal structure.

We can see that our polymers with smaller thermoresponsive blocks form larger particles and polymers with larger thermoresponsive blocks form smaller particles. As we discussed in the Introduction the self-assembly of amphiphilic block copolymers into particles is given by an equilibrium between the attractive and repulsive forces, which can be characterised by the tendency to decrease or increase the contact of the polymer chains with solvent molecules. [23] Based on our measurements we formulated a hypothesis about the internal structure and formation of particles from our copolymers. This could be described analogously to the plum pudding model of the atom. Majority of the volume of the nanoparticle is taken up by swollen hydrophilic blocks hydrated by water molecules and extended in mostly aqueous environment. This forms our hydrophilic gel or "the pudding" and within it are placed the smaller "plums" of hydrophobic blocks aggregating noncovalently together to minimize their contact with the aqueous environment, as depicted in **Figure 12**. This behaviour has been observed in other copolymers as well. [102] The internal structure is dependent on the ratio of the polymer blocks as we observe that if the polymer possesses the inverted ratio of block sizes and its hydrophilic block is shorter than the hydrophobic one, then the interwoven net of hydrophilic chains is not as strong and unable to hold larger structures together leading to formation of smaller particles.
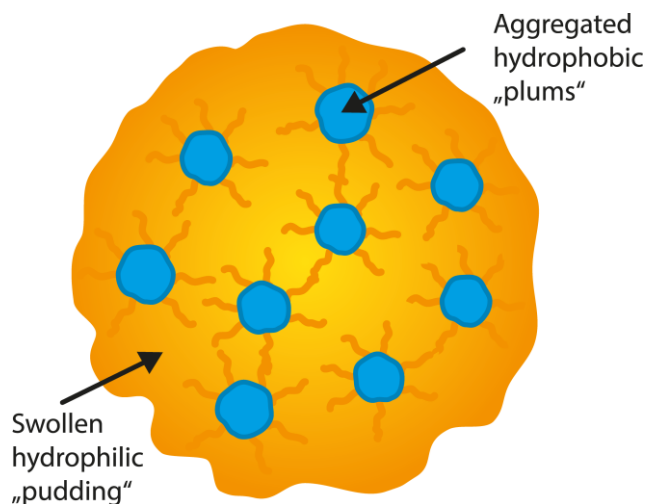

Figure 12 *Hypothesized plum pudding model of the self-assembled polymer nanoparticle.*

3.1.3 Testing biocompatibility and conclusions

The HF3 and MF3 samples were also investigated with regard to their cytotoxicity and haemolytic properties to assess their primary biocompatibility. Their cytotoxicity was shown to be low enough that they might be possibly used for biomedical purposes and at concentrations relevant for biomedical applications they also caused no haemolysis even after 24-h incubation. [98]

To confirm the intended applicability of the obtained polymer nanoparticles of copolymers MF3 and HF3 as fluorine MRI contrast agents ^{19}F NMR measurements were conducted and confirmed that the nanoparticles above T_{CP} at body temperature 37°C still provide sufficient ^{19}F NMR signal. [98] Additional ^{19}F MRI and *in vivo* measurements were made in a separate study by an affiliated research group concluding the studied copolymer systems have promising properties for cell tracking, tumour therapy and diagnosis. [61]

To conclude, in the first phase of our research we confirmed that the prepared copolymers were capable of self-assembly into nanoparticles in aqueous solution after heating above the T_{CP} and through investigation with scattering and microscopic methods we proposed an internal structure model. We also conducted studies which have shown the potential of these self-assembled systems to be used as ^{19}F MRI contrast agents in bioapplications.

The hypothesized "plum pudding model of a nanoparticle" was basis for our further investigation of the internal structure of the obtained nanoparticles of copolymers MF3 and HF3. While it was shown to be a suitable starting point, we ultimately uncovered a somewhat different internal structure of our nanoparticles as discussed in the following section 3.2.

3.2 Detailed analysis of the internal structure of self-assembled particles of PHPMA-*block*-PDFEA and PMeOx-*block*-PDFEA

3.2.1 Research motivation

From the samples investigated in the first phase of the research we selected two, the copolymers MF3 and HF3, which we considered most suitable for the bioaplications because of their size and internal structure. Their cytotoxicity and haemolythic properties were also favourable from the biocompatibility standpoint and

they were shown to provide measurable ^{19}F NMR and MRI signals. So in this phase of research we focused solely on these two copolymers.

Internal structure of nanoparticles is one of the key factors determining their capability to carry drugs or function as a signaling source as it influences their behaviour in biological environment. The aim of this part of research is therefore uncovering internal structure of our nanoparticles and expanding the understanding obtained in the first phase of research. To fulfill this goal the analysis carried out in the section 3.1 was expanded to cover additional advanced techniques, such as small angle X-ray and neutron scattering and ^{1}H and ^{19}F NMR spectroscopy including DOSY and NOESY studies.

3.2.2 Expanded DLS analysis

We carried out DLS measurements of the dependence of size distribution of our samples on temperature and improved our analysis by increasing graphical resolution of the resulting size distributions. This time in addition to pure water (H_2O) we also carried out our measurements in heavy water (D_2O) and in a 140 mM phosphate buffered saline (PBS). The results in D_2O as solvent were useful for comparison to the results from SANS measurements and NMR measurements as both were by necessity carried out either in pure D_2O or with it mixed into the solution. The results from experiments with PBS as a solvent were used as a reference for biological studies and to gain a better estimate how the copolymers could behave in a biological environment which PBS is more alike to than pure water. The data were processed into three dimensional graphs of the dependence of size distribution on temperature and we obtained the hydrodynamic radii R_h of the present particle populations as well as the cloud point temperatures T_{CP} for our samples in all the solvents. The resulting graphs are shown in **Figure 13**. Anomalous micellization was observed in all the samples as an abnormal increase in measured intensity at T_{CP} which is in accordance with previous observations. In all experiments formation of larger particles above T_{CP} can be observed same as before. Because of the difference in the behaviour of the two copolymers, which is discussed below, their measured T_{CP}s and R_hs of particle populations are presented in separate tables (**Table 4** and **Table 5**) for improved legibility.

	R_h [nm]		
Solvent	Unimers	Assemblies	T_{CP} [°C]
H₂O	5.9	50	23
D₂O	5.3	74	23
PBS	5.5	74	21

Table 4 *Measured hydrodynamic radii R_h for unimer and assembly populations, and cloud point temperatures T_{CP} of copolymer PHPMA-PDFEA with block ratio 1:2 (HF3) in H₂O, D₂O and PBS based on DLS experiments. Adapted from [53].*

Solvent	R_h [nm]						T_{CP} [°C]
	below T_{CP}			above T_{CP}			
	I	II	III	1	2	3	
H₂O	4	27	-	11	47	-	33
D₂O	4	21	131	9	46	-	25
PBS	4	17	99	9	32	185	31

Table 5 *Measured hydrodynamic radii R_h for particles in populations below (I, II, III) and above (1, 2, 3) the T_{CP}, and cloud point temperatures T_{CP} of copolymer PMeOx-PDFEA with block ratio 1:2 (MF3) in H₂O, D₂O and PBS based on DLS experiments. Adapted from [103].*

As the copolymers HF3 and MF3 differ in their hydrophilic blocks, their interaction with the various solvents was also different. While the reaction of the copolymer MF3 to changes in solvent polarity and composition is easily observable from the measured intensity distributions, the reaction of the HF3 copolymer is much smaller. This also documents the importance of obtaining comparative results for different used solvents as the external environment also influences the resulting properties of the self-assembled system.

The copolymer HF3 responded to the changes in solvent only by a shift of the particle size (R_h), narrowing of the particle populations and a slight shift of the point of thermally induced self-assembly (T_{CP}).

In comparison the MF3 copolymer formed additional populations not previously observed as a result of change in the solvent. An additional larger particle population appeared below the T_{CP} in D₂O, and one additional population of larger particles appeared above the T_{CP} in the PBS solution. Given that we are working with the intensity-weighted distributions these newly formed larger populations do not represent a significant change in the overall composition of the sample but are noteworthy nonetheless. However, a significant shift of the T_{CP} for the different

solvents was observed for the MF3 copolymer which could potentially have significant ramifications for the bioapplications of this thermoresponsive copolymer.
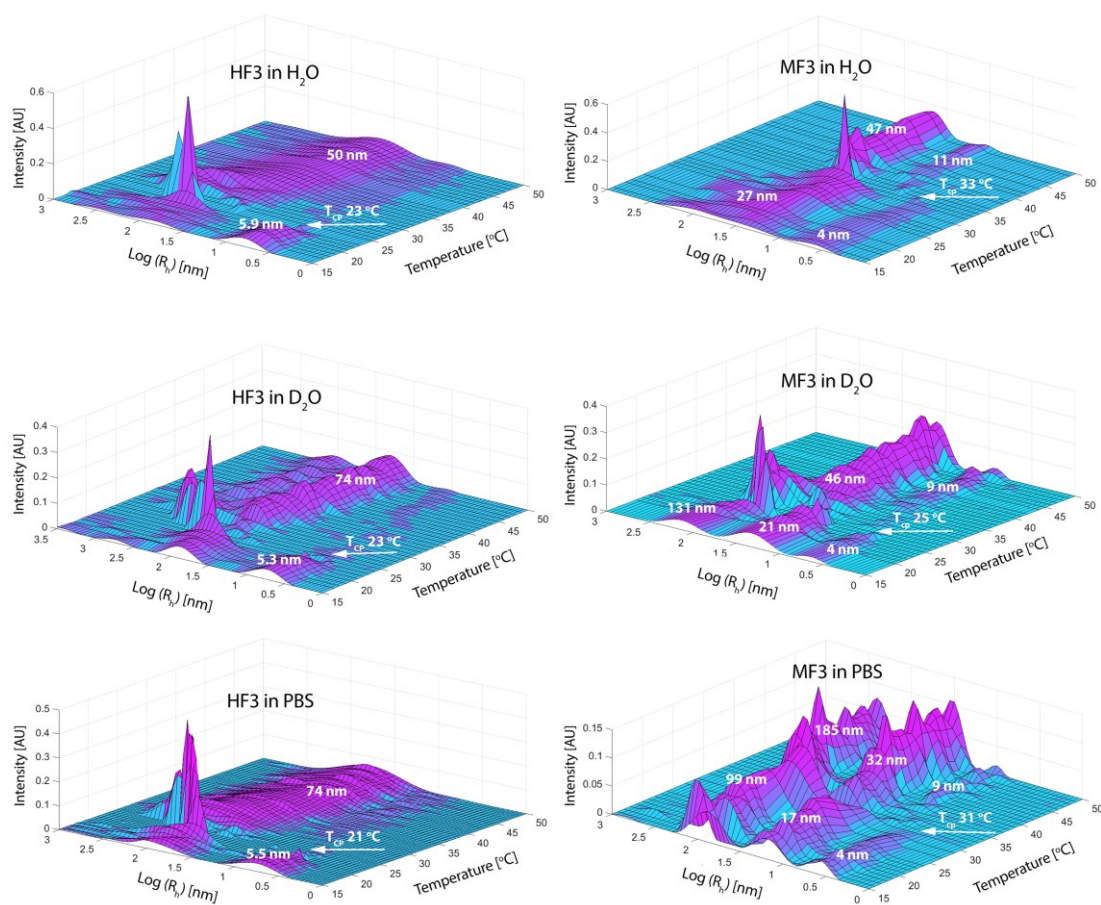

Figure 13 Temperature dependence of intensity-weighted size distributions obtained from DLS of our copolymer samples in H₂O, D₂O, and PBS. Adapted from [53, 103].

3.2.3 Small angle X-ray scattering experiments

Both copolymers in PBS were further investigated by SAXS to obtain a more detailed information on the internal structure and self-assembly processes of the observed particles.

As can be seen from the scattering intensity profiles shown in **Figure 14**, the behaviour of the copolymers in the PBS buffer at lower (blue and green symbols) and higher (red and black symbols) temperature is completely different. In all cases we are observing a complex state of the polymer chains at different points of phase behaviour. In order to describe the objects and obtain parameters of the shape we had to use a combination of several models for the individual curves and their parts. It is important to note that the static scattering methods such as SAXS and SANS observe all the

particle populations at once and their contribution to the overall result is weighted based on the amount of radiation they scatter, which is made yet more difficult because of the different contrast factors between the different types of radiation. As such for the samples with multiple populations the data have to be interpreted very carefully with reference to results obtained by other methods.
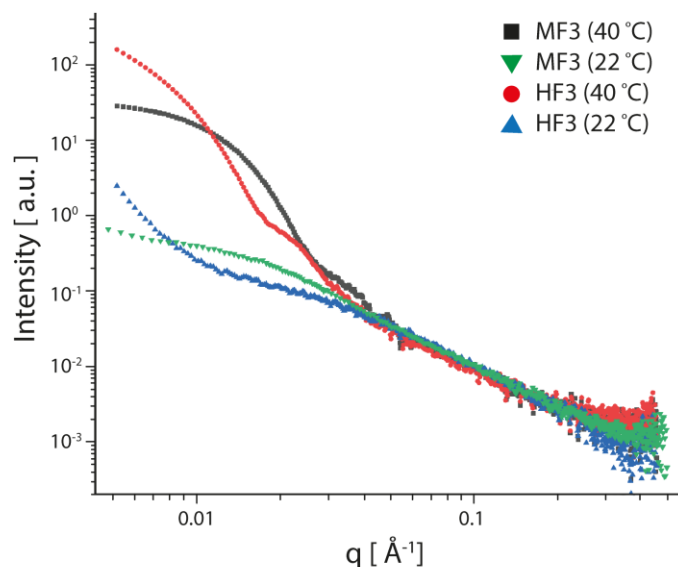
Figure 14 Small angle X-ray scattering intensities as a function of the scattering vector at different temperatures for the samples HF3 and MF3. Adapted from [53, 103].

For the copolymer MF3 the scattering curve in the low-q range at lower temperature exhibits an uprise indicating existence of larger particles which is in agreement with the DLS also showing larger particles even below T_{CP}. These particles are however too big for analysis using the available data. In order to describe data at lower temperatures for the higher q-range, we utilized a generalized Gaussian coil function. The polymer sample exhibits Flory exponent approximately 0.52 which means the polymer chains are in a good solvent with relaxed and well-solvated chains. This observation is in good agreement with SANS results we discuss in section 3.2.4. The fit for sample below the T_{CP} provided resulting radius of gyration R_g as 12.07 nm.

The overall behaviour of the MF3 copolymer in PBS above the T_{CP} where we can expect to observe self-assembled structures could be described as a loose sphere

with R_g of 15 nm and an internal structure represented by Gaussian chains. The radius of gyration of internal coils was fitted as 1.3 nm.

From the obtained data we were able to calculate the molar weight of the swollen particles above the T_{CP} and their swelling degree as described in article [103]. The swollen molar weight was calculated as $M_W = 3 \cdot 10^6 g \cdot mol^{-1}$ and the swelling degree was found to be almost 80%. From these results we attempted to estimate the aggregation number (N_{agg}) of the investigated particles, which gave us $N_{agg} \doteq 122$.

Given the multiple particle populations present in our samples according to DLS, we estimate the calculated swelling degree represents the overall property of the particles of MF3 and their affinity to water. The calculated aggregation number is in range expected for micellar architecture of nanoparticles and thus most likely describes particles in population 1 as observed in DLS, showing them to be micelles. This result is interesting as it significantly furthers our previous observations based purely on light scattering techniques. The calculated R_g above and below the T_{CP} can not be reliably assigned to any one population however its growth at higher temperature documents the self-assembly into larger nanoparticles.

For the results of copolymer HF3 it is important to note that the scattering curve obtained at the lower measurement temperature (22°C), which is very close to its T_{CP}, carries information from the process of self-assembly of the copolymer. The lower measurement temperature for SAXS was chosen as the lowest temperature the instrument was able to achieve under the given atmospheric conditions.

The scattering curve obtained at lower temperature had to be once again separated into two contributions. The increase in intensity at the lower q-range corelates with presence of larger aggregates which corresponds to DLS results. Due to the limits of the experimental equipment available it was only possible to estimate the radius of these larger particles during the self-assembly process as larger than 52 nm. For this the mass fractal function was used as a general model. The mass fractal dimension calculated for this model was 2.6 which suggests dendritic-like or swollen object. This estimate is in good agreement with the calculated swelling degree as discussed below. The higher q-range data were fitted by a model for the generalized Gaussian coil. The uncovered radius of gyration around the T_{CP} was found to be 4.65 nm for the particles fitted by this model and the obtained Flory exponent ν was around 0.52 which suggests that these copolymer chains were still in good solvent,

relaxed and well solvated, as discussed in the section 2.2.2. So, these measured particles are still in the moment just before the phase transition to the aggregated state above the T_{CP}. This is in agreement with the results obtained form the DLS and SANS measurements.

The particles above T_{CP} were described as loose spheres with the radius of gyration $R_g = 24\ nm$ whose internal structure can be fitted as Gaussian chains of $R_g = 1.8\ nm$. The swollen molar weight was found to be $M_W = 4.28 \cdot 10^7 g \cdot mol^{-1}$ and the swelling degree has been calculated to be approximately 34 %. This documents once again a large amount of water inside the particles. An estimate of the aggregation number of the particles above the T_{CP} is approximately 831 which would suggest a different structure then micelle but rather a vesicle or nanogel which is in line with the previous conclusions.

3.2.4 Small angle neutron scattering experiments

The data obtained from the SANS experiments were analysed analogously to the SAXS data as two combined models were needed to describe the scattering curves which are shown in **Figure 15**. The sizes obtained from these measurements were in good agreement with the SAXS results, especially considering the different properties of PBS used in SAXS experiments and D₂O in SANS experiments as solvents and their influence on the self-assembly behaviour of the copolymers.
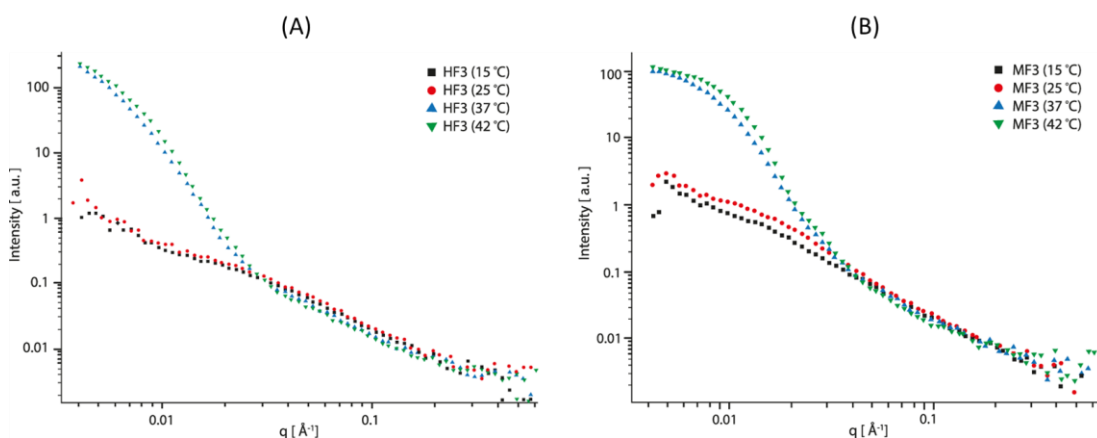
Figure 15 *Small angle neutron scattering intensities as a function of the scattering vector at different temperatures for the samples HF3 (A) and MF3 (B). Adapted from [53, 103].*

From the measurements at different temperatures, we obtained data on the evolution of Flory exponent ν of the present polymer chains behaving like Gaussian coils. The Flory exponent for the HF3 sample shifted from $\nu = 0.580$ at 15°C to $\nu = 0.420$ at 42°C and the Flory exponent for the MF sample shifted from $\nu = 0.560$ at 15°C to $\nu = 0.368$ at 42°C. This is graphically represented in **Figure 16**. The observed decrease of the Flory exponent is in accordance with general polymer theory as discussed in section 2.2.2 and means that the PDFEA block is hydrophilic while the sample is at temperatures lower than T_{CP} and becomes gradually more hydrophobic as the temperature increases.
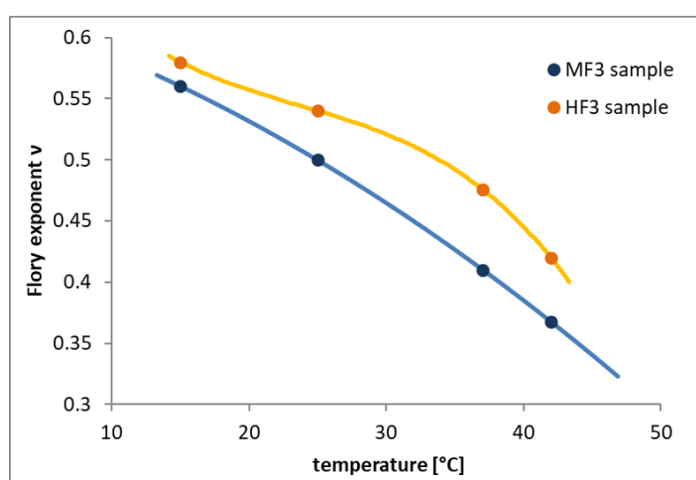
Figure 16 The measured (points) and interpolated (lines) evolutions of Flory exponent value with rising temperature as calculated from SANS experiments for copolymers MF3 and HF3. Adapted from [53, 103].

Based on the results of all the scattering data we conclude that particles in population 1 of the MF3 sample in PBS are micelles and population 2 of MF3 as well as population A in HF3 in PBS are highly swollen aggregates.

3.2.5 Nuclear magnetic resonance investigation

To investigate the internal structure of the self-assembled particles we carried out a set of NMR experiments observing several behaviours accompanying the self-assembly of polymer chains into particles. For the ^{1}H NMR spectra the assignment of individual protons was performed as depicted in **Figure 17** and **Figure 18**.
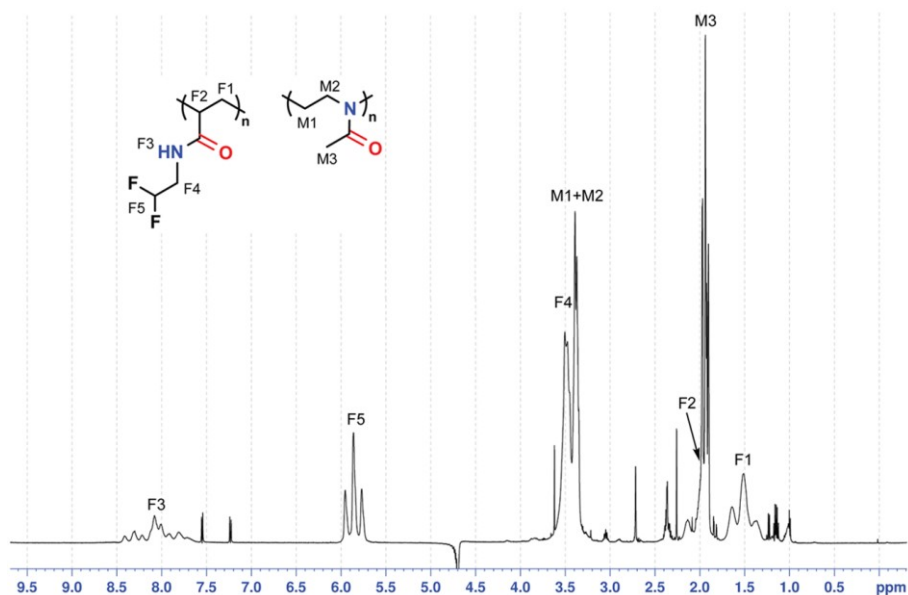
Figure 17 Signal assignment of MF3 copolymer sample. [1]H spectrum acquired at 25°C with assigned signals. Adapted from [103].
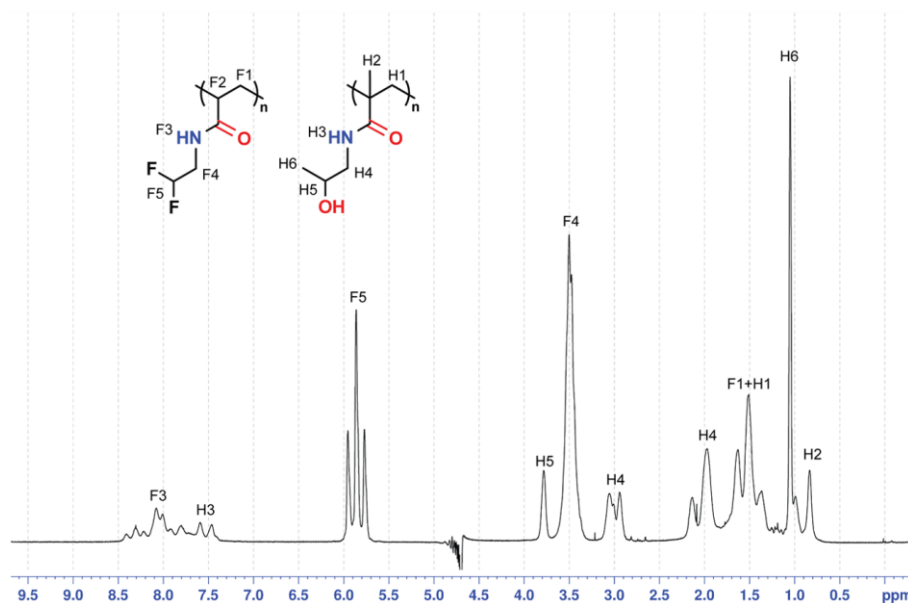
Figure 18 Signal assignment of HF3 copolymer sample. [1]H spectrum acquired at 25°C with assigned signals. [53]

We monitored the signal intensities in ^{1}H NMR spectra with increasing temperature for separate hydrogen atoms in individual copolymer blocks. The results are presented in **Figure 19**. Generally, when a polymer chain collapses, phase separates and forms rigid particles, its NMR signal should disappear and only the mobile polymer chains still dissolved and able to move freely are observable.

In the measured ^{1}H spectra we observed that while the signal intensities of the thermoresponsive PDFEA blocks decreased significantly between the state below and above the T_{CP} there was no significant change observed in the hydrophilic PHMPA and PMeOx blocks (the present variations are caused mainly by the overlap of the signals with hydrogens from the PDFEA block). These results suggest that above the T_{CP} the PDFEA part of the copolymer chain forms a rigid part of the particles while the PHMPA/PMeOx parts of the chains remain flexible.
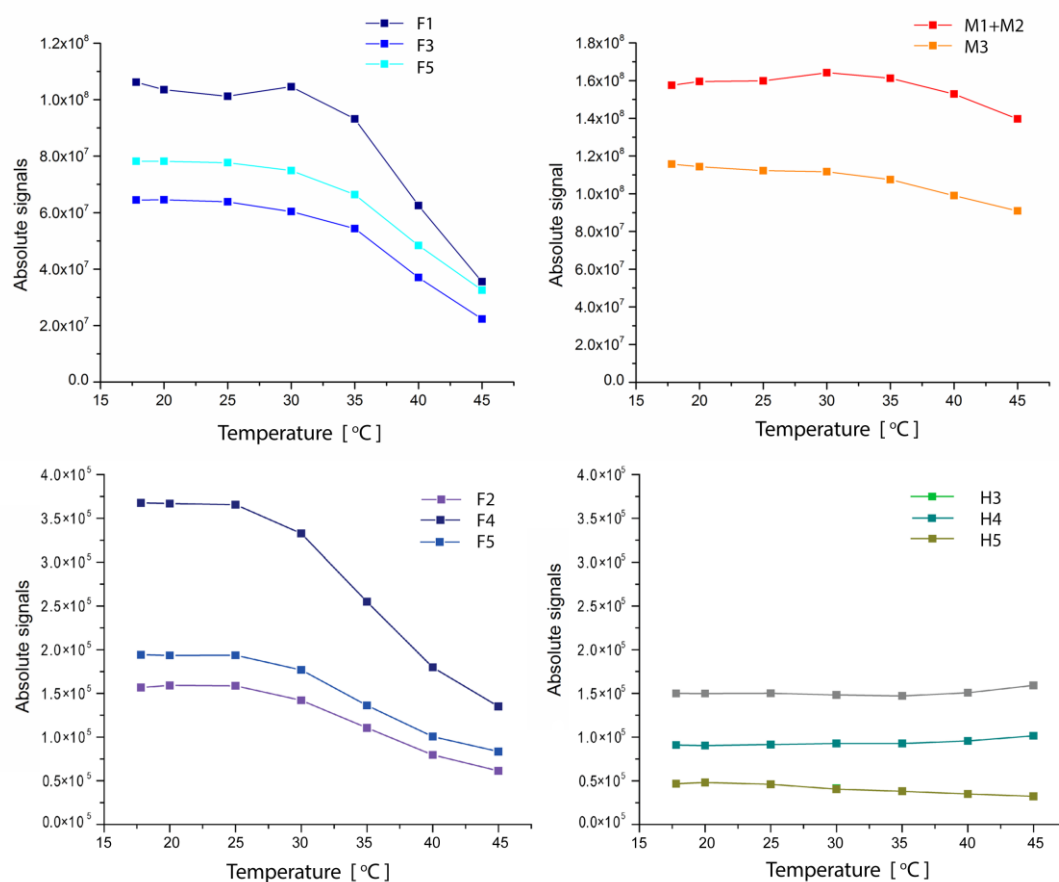
Figure 19 *Temperature dependence of signal integrals from ^{1}H NMR spectra of MF3 (top row) and HF3 (bottom row) copolymers and their thermoresponsive PDFEA parts (left column) and hydrophilic PMeOx/PHPMA parts (right column). Adapted from [53, 103].*

As stated in section 2.3.6, NOESY spectra are a tool to detect close spatial proximity of hydrogen atoms that are separated by no more than 6 Å. The most important parts of NOESY spectra measured for our samples are presented in **Figure 20**. The observed cross-peaks of amide protons F3 of PDFEA block show their close proximity to all other protons of the fluorinated block. In the HF3 copolymer the

same proton does not show close proximity with the PHPMA protons. For the MF3 copolymer the overlap of observed peaks brings large ambiguity into the data interpretation of proximity of F3 to the PMeOx block.
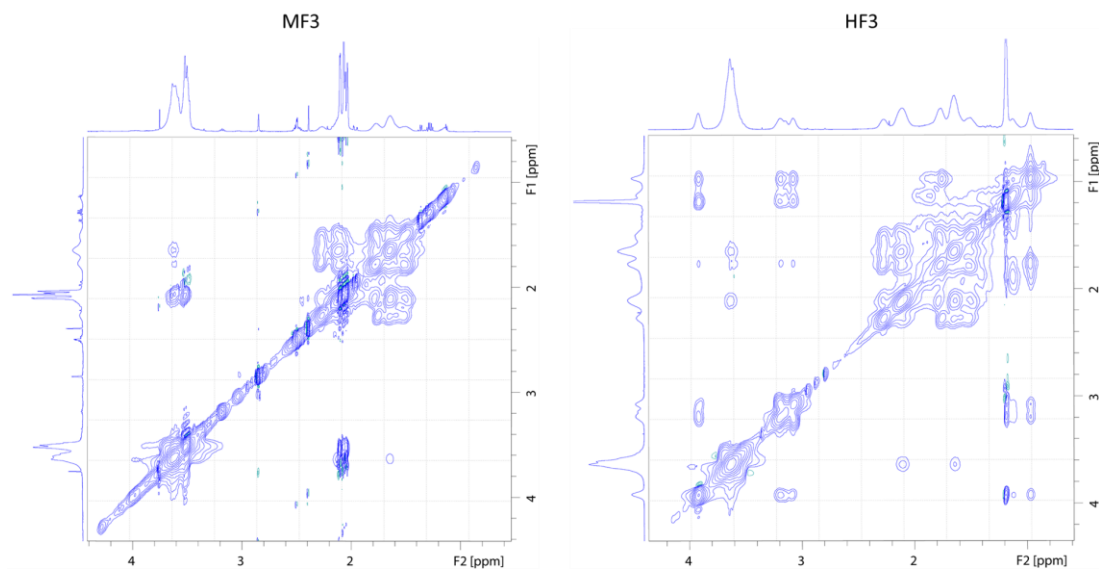
Figure 20 *The most important parts of NOESY spectra acquired for MF3 and HF3 samples. Adapted from [53, 103].*

In case of the HF3 copolymer, cross-peaks were detected also between F4 and F1/F2 protons a well as between H2 and H4/H5 protons. As these atoms are relatively distant in the polymer molecule these results speak of close contact of the side chain groups with the backbone chain of the copolymer. These observations could suggest a hydrogen binding scheme as depicted in **Figure 21** where two sidechains form hydrogen bonds with each other while being flipped in opposition to one another. An arrangement like this brings the sidechain end-groups to the proximity of the polymer backbone as observed in the results.

No interaction between different co-polymer blocks has been observed. The sidechains interact exclusively within sidechains of the same type of block. All the observed interactions are present already in the solvated state of polymers, before the aggregation. NOESY spectra at lower and higher temperatures are basically identical which most likely means in these NOESY spectra we are not observing proton signals from the fully aggregated particles.
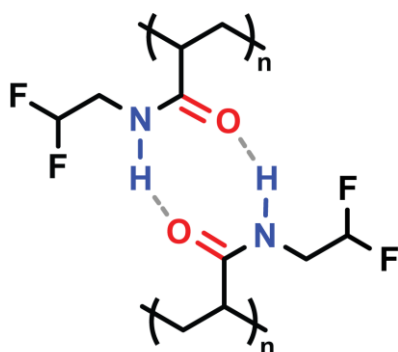
Figure 21 *Suggested hydrogen binding scheme between PDFEA polymer blocks.* *[103]*

From the beginning the studied copolymers were intended to be potentially used as ^{19}F MR-imaging contrast agents. To test their ability to provide a measurable signal, ^{19}F NMR spectra of the polymer samples were acquired and one broad featureless signal was observed around −122.7 ppm (**Figure 22 (A)**). The measured integral intensity of this peak decreased to 70% and 80% for HF3 and MF3 copolymers, respectively, when heated from 20°C to 45°C (**Figure 22 (B)**). This decrease is much less significant than the decrease of the proton signal of the fluorinated block detected in the ^{1}H NMR experiments (**Figure 19 (left)**). This difference could be explained by different relaxation properties of ^{1}H atom in CHF_2 group which differ from ^{19}F atoms. Thus, ^{19}F NMR may allow to observe bigger polymer aggregates than ^{1}H NMR spectroscopy.
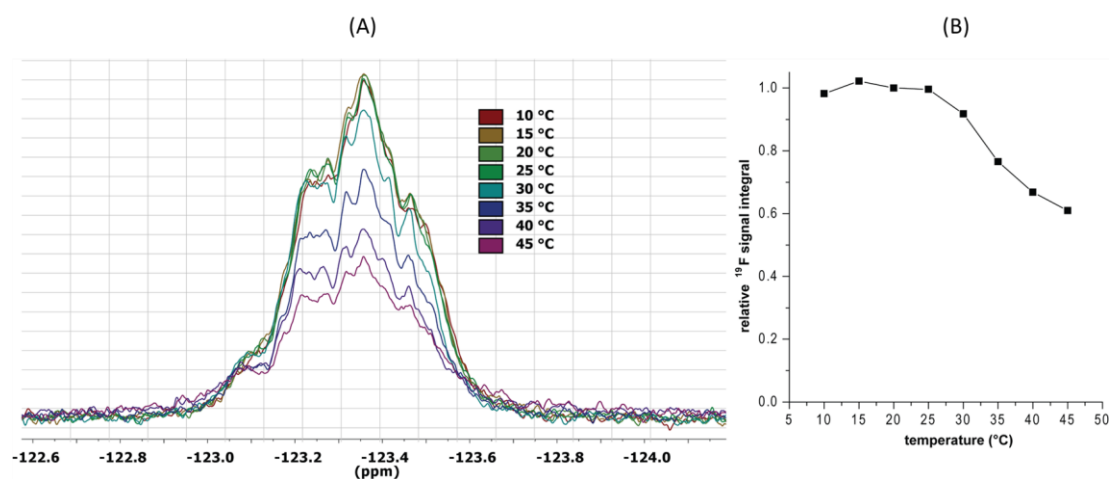
Figure 22 *(A) Stacked ^{19}F NMR spectra of HF3 copolymer at different temperatures. (B) The relative integral of the detected ^{19}F signal as a function of temperature. These results are illustrative also for the MF3 sample. Adapted from [53].*

52

We measured translational self-diffusion coefficients through the DOSY experiments. In the DOSY spectra, each signal describes a measure of diffusion properties in relation to the individual hydrogen atoms. When the whole molecule moves as a unit, that is the whole particle either as a single chain or as a part of a polymeric assembly, all its individual proton signals should provide the same diffusion coefficient with regard to that shared movement. The diffusion coefficients observed in the samples are thus a combination of translational diffusion which should be virtually the same for both blocks and the "self-diffusion" caused by deformations of the polymer chain.

As expected, the observed values of individual signals within one copolymer block are the same. However, the diffusion coefficients measured for the hydrophilic PHMPA/PMeOx blocks are mostly higher when compared to those of the thermoresponsive PDFEA block as shown in **Figure 23**. The diffusion coefficients for the hydrophilic and thermoresponsive block also behave differently with the increasing temperature of the sample. Several things are happening in the sample with the increasing temperature. The viscosity of the sample decreases and thus the diffusion coefficient increases as described by the Stokes-Einstein equation. The thermoresponsive blocks become more hydrophobic and the free copolymers self-assemble into larger particles. This leads to following observations.
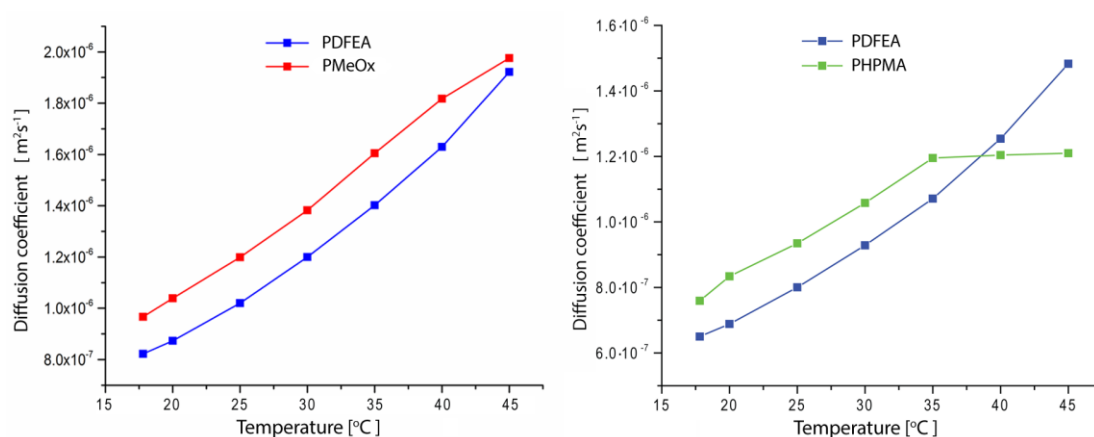
Figure 23 *Self-diffusion coefficients determined for MF3 (left) and HF3 (right) copolymers as a function temperature. Adapted from [53, 103].*

The apparent diffusion coefficient of PDFEA block accelerates its increase with temperature as the PDFEA blocks phase separate from the solvent and the protons

which would exhibit lower diffusion coefficient do not provide so much signal as their relaxation is hindered inside the condensed hydrophobic block, as seen in **Figure 19**.

The overall apparent diffusion coefficient of the PMeOx/PHPMA blocks slows down its increase with the rising temperature. The origin of this can be seen in the slower decrease of integral intensity of PMeOx/PHPMA signals in the proton spectra (**Figure 19**) in comparison to the PDFEA signals. This means that the hydrogens of the hydrophilic blocks provide relatively strong proton signal even inside the particles whose translational diffusion is slower than that of the free polymers, which is then reflected in the overall measured diffusion coefficient. The DOSY measurements thus confirm that the hydrophilic PMeOx/PHPMA blocks of our copolymers remain mobile and flexible even after they self-assemble into particles.

An interesting note is that the apparent diffusion coefficient of the PHPMA block becomes nearly constant and its increase is almost fully stopped after reaching high enough temperature. This is most likely due to the aggregation as its diffusion becomes limited and remains nearly constant. This difference between the PMeOX and PHPMA is also in line with the SAXS results as the aggregated HF3 nanoparticles above the T_{CP} showed a much lower content of water then the MF3 nanoparticles which could explain why their movements are more limited.

The results obtained from the NMR experiments show that even though the thermoresponsive PDFEA blocks form aggregates and their ^{1}H NMR signal decreases as they phase separate and their mobility is restricted their ^{19}F NMR signal exhibits a much smaller decrease meaning that the self-assembled particles can be detected through the ^{19}F NMR. This has been shown to be true in a separate *in vivo* study on mice. [61]

3.2.6 Summary of the results investigating the internal structure of the particles

In concurrence with the first phase of the research it was observed that in all investigated solvents H_2O, D_2O and PBS the fluorinated block copolymers PMeOx-*block*-PDFEA and PHPMA-*block*-PDFEA form complex nanoparticular structures both above and below the T_{CP}. Below the T_{CP} the molecularly dissolved unimers are in equilibrium with larger aggregates which most likely form around the free chains of thermoresponsive homopolymer leftover from synthesis. The presence of these

homopolymer chains is evidenced even by the anomalous micellization observed at the T_{CP}. Above the T_{CP} self-assembled particles are formed whose properties are influenced by the specific solvent in which they are suspended. This influence is more prominent in the PMeOx-*block*-PDFEA copolymer than in the PHPMA-*block*-PDFEA copolymer. As could be expected the difference between the hydrophilic blocks of the copolymers has a major impact on resulting properties of the copolymer nanoparticles.

In the NMR studies it was found that the hydrophilic and hydrophobic blocks do not come into close contact and do not interact with each other. While the thermoresponsive PDFEA blocks aggregate above T_{CP} into a condensed phase they were proven to be able to provide a measurable ^{19}F NMR signal even under these conditions. Meanwhile the hydrophilic blocks were shown to remain mobile even after self-assembly into the nanoparticles.

Based on the results obtained through all the methods we modified our previous hypothesis on the internal structure of the nanoparticles of copolymers MF3 and HF3. While previously we considered PDFEA to form separate condensed hydrophobic cores (the abovementioned hydrophobic plums) it now seems most likely that the PDFEA blocks form an interconnected hydrophobic network penetrating throughout the whole particle. The individual PDFEA blocks are most likely interconnected by hydrogen bonds and the calculated Flory exponents from SAXS and SANS experiments show that the fluorinated blocks are being forced out of the aqueous environment through the hydrophobic interactions. This network is then probably shielded by highly swollen hydrophilic chains which are binding large amounts of water inside intraparticular compartments. This improved model of the internal structure is schematically shown in **Figure 24**. The SAXS measurements even show that the PMeOx chains inside the nanoparticles behave like coils in a good solvent, while the DOSY experiments show that the PHPMA chains are somewhat hindered in their movement in particles above certain temperature. Both are in good agreement with the content of water and swelling of the particles uncovered by SAXS.
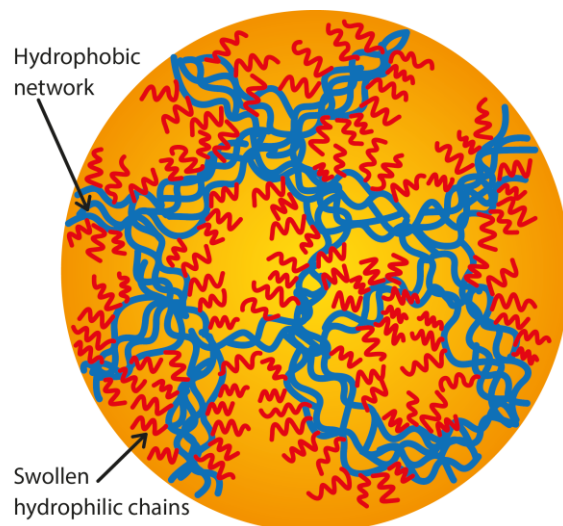
Figure 24 *Newly hypothesized internal structure of the self-assembled polymeric nanoparticles as an interconnected hydrophobic network shielded by swollen hydrophilic chains. Adapted from [53, 103].*

3.3 Critical comparison of self-assembly properties of block and gradient copolymers of 2-methyl-2-oxazine and 2-propyl/butyl-2-oxazoline

3.3.1 Polymer description and sample preparation

We further designed a new set of copolymers with block and gradient architectures and investigated their properties to assess their similarities and differences. As copolymers with gradient architecture are not as widely used or investigated in biomedical research few comprehensive studies are available and so a detailed side-by-side comparison can bring valuable insight into their prospects for bioapplications. We decided to use the 2-methyl-2-oxazine (MeOzi) as a hydrophilic monomer and 2-propyl-2-oxazoline (PrOx) or 2-butyl-2-oxazoline (BuOx) as the thermoresponsive or hydrophobic monomers, respectively. [104] This choice was made in light of recent studies which showed that both block and gradient copolymers can be formed by these monomers. [104, 105] The poly(2-alkyl-2-oxazoline) (PAOx) [105-111] and poly(2-alkyl-2-oxazine) (PAOzi) [112-115] based polymers were also shown to exhibit properties as favourable for bioapplications as some long established polymers used in biomedical research such as the hydrophilic poly[(*N*-(2-hydroxypropyl)methacrylamide] (PHPMA) [116, 117] and poly(ethylene oxide) (PEO), [118] or the hydrophobic poly(ε-caprolactone) [119, 120] and poly(lactic acid)

56

[121]. The copolymers were synthetized with the hydrophilic to hydrophobic/thermoresponsive monomer ratios 2:1, 1:1 and 1:2 as in previous study to compare the differences between the variants and to confirm the system is adjustable for specific requirements.

The nanoparticles investigated in this study were prepared using a nanoprecipitation method. The polymer was first dissolved in acetone and then added dropwise into a PBS solution which was being stirred intensely. The acetone was then evaporated and additional PBS was added to adjust the resulting concentration to 1 mg·ml^{-1}. The nanoparticles with loaded drug were prepared in the same manner but a small amount of rifampicin (usually 0.1 mg·ml^{-1} unless stated otherwise) has been dissolved in acetone together with the polymer. The notation of samples with loaded drug is an -L sign added to the name of the sample.

The rifampicin was chosen as a model drug because it is already in use as a first line antituberculotic, it is relatively lipophilic [122, 123] and as such suitable for loading into hydrophobic core of particles. It is also able to form a large number of hydrogen bonds as it has many acceptor/donor moieties for hydrogen bonds as shown in **Figure 25**, enabling it to interact with the amphiphilic copolymers.
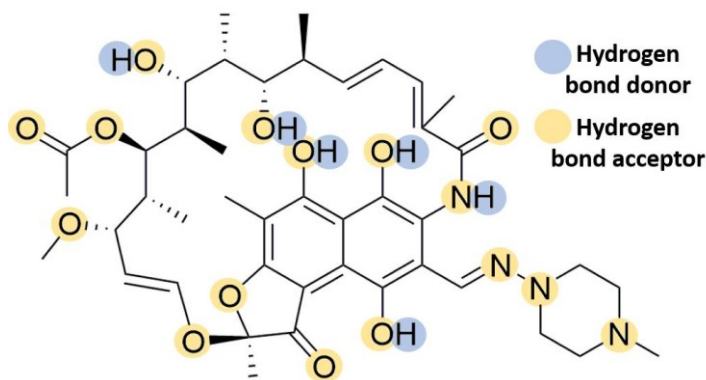
Figure 25 *Structure of rifampicin in its neutral form with schematically marked possible hydrogen bonding sites. [27]*

The properties of nanoparticles obtained from nanoprecipitation of the prepared copolymers were investigated with a wide array of analytical methods foremost of which was the DLS followed by SAXS, TEM and NMR spectroscopy.

The synthesis gave us a large set of 12 copolymers. Their compositions and code designations are listed in **Table 6**. The codes denote the copolymer chain internal architecture (B - block, G - gradient), if the thermoresponsive or hydrophobic

monomer present is PrOx (P) or BuOx (B) and what is the ratio of the hydrophilic to thermoresponsive or hydrophobic monomers (1 - 1:2, 2 - 1:1, 3 - 2:1).

Code	Composition	%MeOzi/%BuOx, PrOx	M_W [kg·mol^{-1}]	Đ
BP1	P(MeOzi-*block*-PrOx) 1:2	33/67	16.8	1.06
BP2	P(MeOzi-*block*-PrOx) 1:1	50/50	12.1	1.07
BP3	P(MeOzi-*block*-PrOx) 2:1	67/33	12.4	1.17
GP1	P(MeOzi-*grad*-PrOx) 1:2	33/67	14.3	1.04
GP2	P(MeOzi-*grad*-PrOx) 1:1	50/50	12.4	1.03
GP3	P(MeOzi-*grad*-PrOx) 2:1	67/33	13.2	1.19
BB1	P(MeOzi-*block*-BuOx) 1:2	33/67	17.3	1.17
BB2	P(MeOzi-*block*-BuOx) 1:1	50/50	14.6	1.14
BB3	P(MeOzi-*block*-BuOx) 2:1	67/33	12.6	1.18
GB1	P(MeOzi-*grad*-BuOx) 1:2	33/67	16.3	1.07
GB2	P(MeOzi-*grad*-BuOx) 1:1	50/50	15.6	1.11
GB3	P(MeOzi-*grad*-BuOx) 2:1	67/33	13.3	1.07

Table 6 *Code, composition and structure of the prepared block and gradient copolymers. The percentual monomer ratio was determined by NMR and the molar weight (M_W) and its dispersity (Đ) were determined by SEC. Adapted from [27].*

3.3.2 DLS analysis

Samples of self-assembled nanoparticles in PBS were prepared from all the copolymers by the abovementioned nanoprecipitation method both without and with the loaded rifampicin drug. This provided us with a total of 24 samples. The size distributions of particles present in them were investigated at a range of temperatures by DLS measurements. Based on this vast set of results we chose the copolymers with the monomer ratio of 1:1 loaded with drug as the most suitable for further research. The thermal evolutions of size distributions for these samples (BP2-L, GP2-L, BB2-L, GB2-L) are shown together in **Figure 26**.
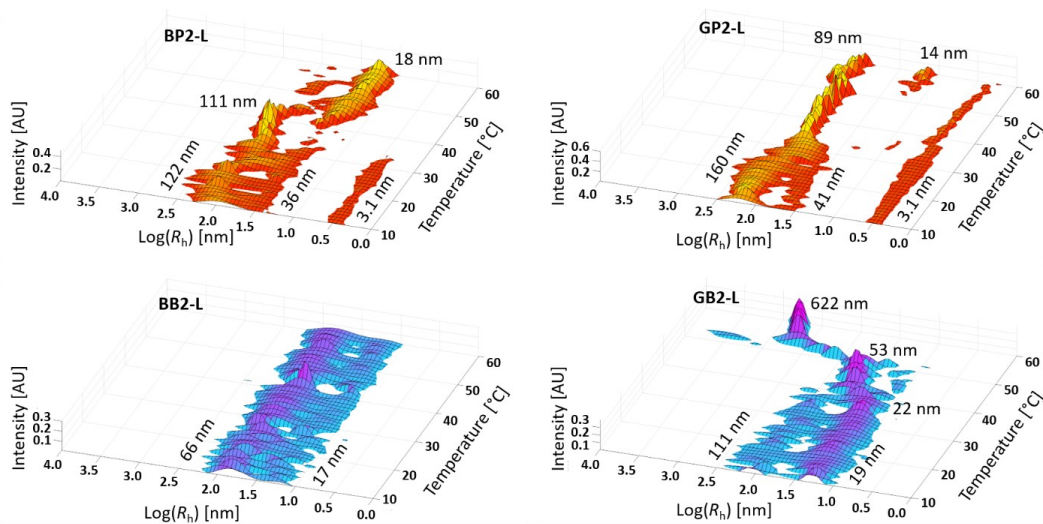
Figure 26 *Temperature dependence of size distributions of the self-assembled systems of the BP2-L, GP2-L, BB2-L, GB2-L copolymers loaded with rifampicin. [27]*

The obtained DLS data show thermal response of some form in many of our samples. We observed two distinguishable types of thermally induced changes.

The first is the self-assembly of molecularly dissolved unimers into nanoobjects. This could be described as typical response of thermoresponsive copolymer at the T_{CP} and, as could be expected based on the properties of used monomers, was observed solely in the PrOx-containing samples. It was distinctly accompanied by the disappearance or significant diminishing of the unimer population.

The second type of response induced by increasing temperature was the aggregation of smaller particles into larger assemblies. The formation of larger aggregates and even macroprecipitation, is in accord with recent findings that the presence of certain salts in the solution (such as those in the PBS) can in certain cases cause polymers to form larger assemblies and even precipitate when heated above a certain temperature as their hydrophilic coronas interact and entangle to form the larger assemblies. [124, 125] The formation of these large aggregated particles and/or macroprecipitation were observed for samples containing both the PrOx and BuOx monomers.

The reversibility of these temperature dependent changes was investigated. After reaching the maximum temperature the samples were quickly cooled and their size distribution was measured again. The changes found to be irreversible were those in samples GB1 and GB1-L. The other samples showed their changes were either fully

reversible or only a small residual population of larger particles was left after cooling, which was negligible in comparison to the reformed population of smaller particles.

The homopolymers PMeOzi, PPrOx and PBuOx and their behaviour in aqueous media with regard to changing temperature was thoroughly investigated in previous study. [104] Only the PPrOx homopolymer exhibited thermoresponsive behaviour and only the PBuOx homopolymer was shown to be insoluble in water at room temperature. [104] This is in agreement with the observed result that only the PrOx-containing copolymers responded by thermally induced self-assembly and upon heating above the T_{CP} transitioned from molecularly dissolved unimers into micelles.

The specific temperature of the thermal response of the samples containing the PrOx monomers varied with the varying ratio of hydrophilic to thermoresponsive monomers in their chain. Their T_{CP} seems to be derived from that of the PPrOx homopolymer ($\approx 25°C$) [107] and for our copolymers it increases with the growing content of the hydrophilic monomer MeOzi in the polymer chain. The copolymers with gradient architecture exhibited higher T_{CP} values than the block copolymers, which could be caused by the presence of the hydrophilic MeOzi monomers among the thermoresponsive PrOx monomers. [126]

For the BuOx-based copolymers there was no clear transition from unimers to micelles measured in the DLS experiments as they did not express the usual thermoresponsive behaviour. As mentioned above, the homopolymers PBuOx and PMeOzi are not thermoresponsive. [104] The thermally induced response observed in the BuOx-containing copolymers can be described as aggregation of the micellar particles prepared before the experiment by nanoprecipitation.

The temperature dependent changes observed in the BuOx samples, if present, can be described either as a steady growth of size of the aggregates or a gradual separation of the population of the smaller particles and decrease in both their size and quantity as they aggregate into larger assemblies, which has been observed for example for samples BB1, BB3, BB3-L. The shrinking of the micellar nanoparticles is most plausibly caused by partial dehydration of the polymers leading to decrease of their size.

The temperatures of the thermal response of all the samples for which they were observed are listed in **Table 7**. The temperatures listed are the points at which first significant representative changes to unimer or aggregate population occurred.

For the PrOx samples this corresponds to the T_{CP}, where unimers self-assemble into micelles and for the BuOx samples, this marks the aggregation of micelles into larger assemblies, as discussed above.

Thermal change temperature [°C]

PrOx samples				BuOx samples		
	Unloaded	Loaded			Unloaded	Loaded
BP1	24	25		BB1	33	*
BP2	33	33		BB2	*	*
BP3	48	49		BB3	38	32
GP1	32	34		GB1	21	24
GP2	*	51		GB2	50	40
GP3	*	*		GB3	40	45

***Table** 7 Thermal change temperatures of the samples with (loaded) and without (unloaded) rifampicin loaded into them. For samples marked * no restructuring changes were observed. Adapted from [27].*

The observations made from the DLS experiments confirm the ratio of monomers in the copolymer has a strong influence on its self-assembly behaviour. Based on the results it can be surmised the T_{CP} for the PrOx-containing copolymers could be fine-tuned by changing the monomer ratio to fit a desired application.

To compare the copolymers in the broadest sense the PrOx-containing copolymers form primarily unimers at lower temperature and then shift towards self-assembled structures with rising temperatures, while BuOx-containing copolymers, which are more hydrophobic, form self-assembled structures from the lowest measured temperatures with the sole exception of the sample GB3 without a drug.

The monomer ratio of the copolymer has significant influence not only on the temperature of the thermal response of the copolymer but on the overall self-assembly and resulting sizes of present nanoparticles as well.

The copolymers with a monomer ratio of MeOzi:PrOx/BuOx 1:2, which have the largest thermoresponsive/hydrophobic part, tend to form the largest aggregates or even phase separate in macroscopic chunks out of the solution at higher temperatures. From these copolymers the ones with gradient architecture show a stronger tendency to form the largest aggregates or fall out of the solution completely. This can be most

likely explained by the presence of hydrophobic units in the hydrophilic shell of the gradient copolymers which destabilizes the smaller particles.

The samples of copolymers with a monomer ratio of 1:1 formed rather well-defined particle populations which is why the drug-loaded samples of these copolymers were chosen as the most representative. The comparison between the BP2-L and GP2-L samples shows that the block copolymer BP2-L is mostly present as unimers at lower temperatures and at higher temperatures it self-assembles into micellar nanoparticles of approximately 18 nm in size. The GP2-L sample on the other hand is mostly molecularly dissolved at all temperatures examined. This difference can once again be ascribed to the incorporation of MeOzi monomers into the PrOx-rich portion of the gradient copolymer leading to its lower hydrophobicity. Both samples BB2-L and GB2-L show presence of micelles for a wide range of temperatures and only the results for GB2-L show the complete transition of these micelles into the larger aggregates at higher temperatures, most probably owing to the presence of BuOx monomers in the hydrophilic MeOzi part of the gradient copolymer.

The samples of copolymers with a monomer ratio of MeOzi:PrOx/BuOx 2:1 and thus the largest hydrophilic part expressed generally lower tendency to self-assemble and were prone to remain dissolved as unimers throughout the whole examined temperature range or self-assemble only at higher temperatures than copolymers with different examined monomer ratios.

The PrOx-containing block copolymer samples BP3, BP3-L formed self-assembled particles at temperatures much higher than physiological and the destabilizing presence of hydrophilic monomers in the thermoresponsive part of their chain caused the gradient copolymer samples GP3 and GP3-L to remain almost exclusively molecularly dissolved throughout the whole temperature range only exhibiting very small changes of their size distributions. Incorporation of the drug into these samples stimulated formation of more compact self-assembled nanoparticles of the gradient copolymers however even then the nanoparticles mostly remained in the minority when compared to the unimers in the sample.

The size distributions of BuOx-containing block copolymer samples BB3, BB3-L showed presence of micelle-like particles together with larger aggregates. An interesting observation was made that the micelle-like particles present in these samples grew smaller with rising temperatures, which is most apparent in the BB3-L

sample. The gradient analogues GB3 and GB3-L expressed a minor thermal response at higher temperatures. The sample without drug remained mostly in the form of unimers but loading of the drug caused it to self-assemble into a significant nanoparticle population that responded to higher temperature by aggregation into larger particles as discussed above.

In **Table 8** we list the sizes R_h representative of the particle population in each of the samples at 37°C. There are three listed particle populations in the table. Population **U** represents the unimers and, given the nature of the intensity plots as described in the introduction, if listed, it represents the majority of the polymer in the sample. Population **I** should be describing singular micelle-like particles and population **II** corresponds to larger aggregates formed by the smaller particles.

	PrOx samples							BuOx samples					
	R_h [nm]							R_h [nm]					
	Unloaded			Loaded				Unloaded			Loaded		
Population	U	I	II	U	I	II	Population	U	I	II	U	I	II
BP1	*	28	430	*	38	391	BB1	*	23	127	*	30	109
BP2	*	*	168	*	*	112	BB2	*	20	75	*	17	62
BP3	3	*	121	3	*	94	BB3	*	28	98	*	29	136
GP1	*	*	2349	*	11	137	GB1	*	*	1050	*	precip.	
GP2	2.9	*	131	3.2	*	109	GB2	*	32	144	*	33	86
GP3	3	*	*	2.4	*	133	GB3	3.2	*	75	*	*	57

Table 8 *Hydrodynamic radii of loaded and unloaded samples at 37 °C (R_h). Particle population:* ***U*** *- uimers,* ***I*** *- micelle-like particles,* ***II*** *- aggregates. Mark * signifies the population was not present at 37°C. One sample macroprecipitated marked as precip. Adapted from [27].*

The results discussed above showed that incorporation of the rifampicin drug changed the self-assembly behaviour in many of our samples. In the samples GP1-L, GP2-L, BB1-L, BB2-L, GB2-L, and GB3-L, formation of particle populations smaller then in their unloaded counterparts was observed and in sample GP3-L loading of the drug even induced the formation of a particle population, not previously present in the unloaded sample. Even though these new self-assembled particles of GP3-L still remained in minority when compared with the unimer population. The copolymers with the gradient architecture seemed to be affected to a greater extent than the block copolymers and the copolymers containing BuOx monomers showed a stronger

response to loading of the drug than the copolymers containing PrOx monomers. These observations thus seem to confirm the hydrogen bonding interactions expected from the rifampicin molecule as it possesses both hydrogen bond donor and acceptor moieties (see **Figure 25**). When loaded into the samples it can induce hydrophobic associations and partial dehydration of the more hydrophobic portions of the copolymers by a combination of hydrophobic and hydrogen bonding interactions between the polymer and the rifampicin molecules. It can be hypothesized that the dehydration effect is more prominent in the gradient copolymers because they contain hydrated MeOzi monomeric units inside their hydrophobic domains. The presence of rifampicin was also shown to have an effect on the CAC, as discussed in the section 3.3.6 below.

3.3.3 *Small angle X-ray scattering analysis*

We chose the most representative samples BB2-L, GB2-L, BP2-L and GP2-L, as discussed above, to be further analysed by SAXS to gain additional insight into the internal structure of the formed nanoparticles as SAXS experiments could be able to provide it. Unfortunately, only the copolymer containing BuOx monomers provided sufficient scattering for analysis. The scattering curves measured for the samples of BuOx-containing copolymers were fitted using SasView [127] software by the raspberry model of a particle, which further supports the hypothesized aggregation of the smaller micelle-like particles into larger assemblies, through their interacting hydrophilic coronas. [124] The parameters of the data fit are presented in **Table 9**.

The raspberry model form factor in the SasView software is given as smaller spheres with a radius of R_{sm} submerged into one larger sphere with a radius of R_{lg}. [128] The described model does not provide the depth of penetration of the smaller spheres inside the larger sphere. Given these limitations the results obtained from the SAXS experiments seem to be satisfactorily in agreement with the results from the DLS experiments. The most valuable information we can derive from the comparison of the SAXS and DLS results is the observation that the micelle-like particles in the samples can aggregate into larger assemblies as their hydrophilic coronas stick to one another, which was previously observed for similar systems. [124]

Sample	R_{lg} [Å]	R_{sm} [Å]	φ_{lg}	φ_{sm}
BB2-L	164	119	0.0308	0.0548
GB2-L	153	90	0.0195	0.0087

Table 9 *Fitting results of the scattering data from the BuOx samples by the raspberry model. R_{lg} and φ_{lg} are the radius and volume fraction of the large spheres, respectively, and R_{sm} and φ_{sm} are the radius and volume fraction of the small spheres, respectively. Adapted from [27].*

The data obtained by the SAXS experiments were further processed by *ab initio* methods to confirm the suitability of the used raspberry model proposed as the internal structure of the investigated particles of BB2-L and GB2-L samples. The DAMMIF [129] and GASBOR [130] software were used together to evaluate the most probable internal structure present in the particles. The results for a set of random seeds for DAMMIF were averaged and then the two models obtained from the softwares were merged to visually confirm the proposed raspberry architecture of the particles of samples BB2-L and GB2-L as shown in **Figure 27**.
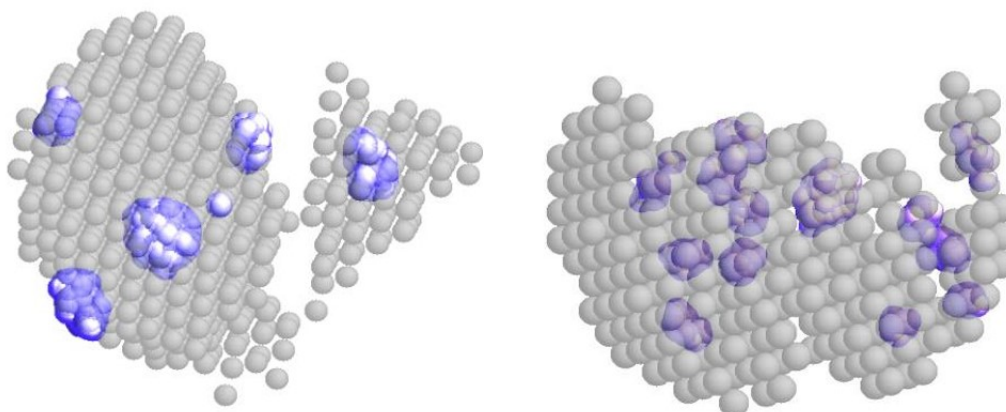
Figure 27 *Superposition of the particle models calculated by the ab initio software DAMMIF (grey spheres) and GASBOR (violet spheres) for samples BB2-L (left) and GB2-L (right). The small grey and violet spheres are individual auxiliary scattering centres used as the smallest calculation units of the models. Together these small spheres represent the real continuous mass of the particle. [27]*

3.3.4 TEM imaging

To further investigate our self-assembled structures, we examined the samples loaded with rifampicin (BP2-L, GP2-L, BB2-L and GB2-L) by TEM. The samples were prepared by nanoprecipitation, same as for the DLS measurements. The resulting

images are shown in **Figure 28**. They serve mainly as a reference to confirm formation of particles with the added benefit of suggesting possible additional information such as particle shape and diameter (D).
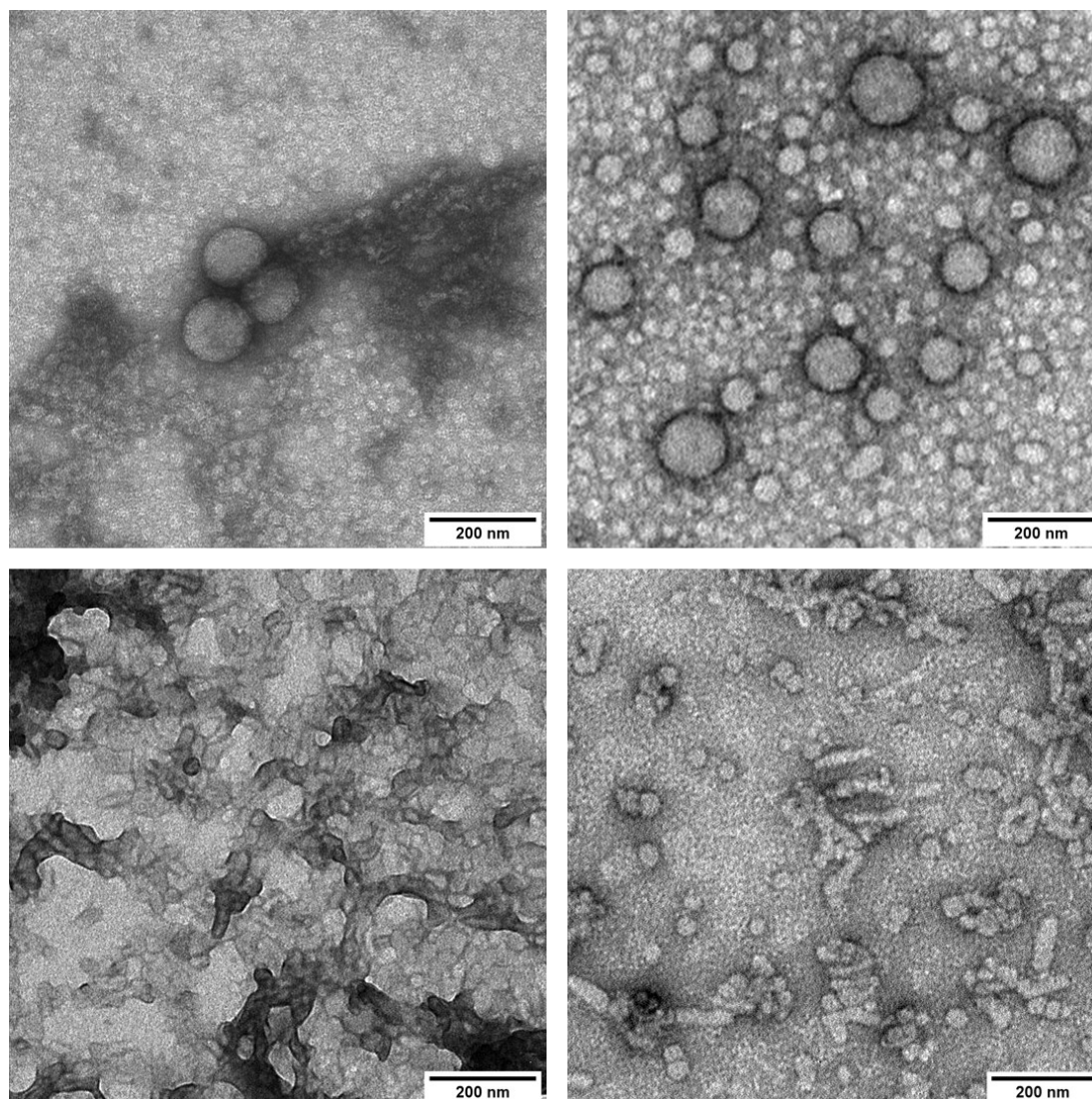
Figure 28 *Negatively stained TEM micrographs showing dried particles of the copolymers BP2-L (top left), GP2-L (top right), BB2-L (bottom left) and GB2-L (bottom right). The samples were prepared from polymer solutions (5 mg·ml^{-1} in 140 mM PBS with 0.5 mg·ml^{-1} rifampicin, pH = 7.4) via a fast-drying method using uranyl acetate (2 µL of a 2 wt. % solution) as a staining agent. [27]*

In sample BP2-L (**Figure 28**, top left) a large number of small spherical particles ($D \sim 50\ nm$) and some larger particles ($D \sim 100\ nm$) were observed which is in good agreement with the DLS results. The analysis of TEM images of sample GP2-L (**Figure 28**, top right) revealed spherical particles with a range of diameters from 50 to 100 nm, and the images obtained for sample BB2-L (**Figure 28**, bottom left) depict

aggregated smaller particles. Images of sample GB2-L (**Figure 28**, bottom right) show spherical particles ($D \sim 40 \ nm$) alongside elongated particles approximately 100 nm in length and 40 nm in width. Overall, the TEM results support our conclusions made based on the DLS.

3.3.5 Nuclear magnetic resonance analysis

To further our understanding of self-assembly of our copolymers we carried out ^{1}H NMR spectroscopy measurements on samples BP2-L, GP2-L, BB2-L and GB2-L. These were prepared by nanoprecipitation into D_2O with 0.1 mg·ml^{-1} of rifampicin. The drug concentration was small enough to be below the detection limit of the NMR spectrometer under the conditions of the used method. Assignment of the spectral signals is depicted in **Figure 30**.

By comparing the ^{1}H NMR spectra measured in D_2O and in deuterated methanol-d4, in which the polymer should be freely molecularly dissolved we see that the signal from D_2O was overall much lower but this decrease in signal intensity was much greater for the thermoresponsive and hydrophobic parts (PrOx/BuOx) of the copolymers than for the hydrophilic MeOzi parts, an example of this is depicted in **Figure 29**. The signal decrease could be linked to the phase separation and solidification of the more hydrophobic monomers into the particle core. This decrease of the hydrophobic signal is also more prominent for the block copolymers than for the gradient copolymers (in the BB2 sample, there was no signal detected from BuOx in the nanoparticles) which suggests that without the hydrophilic monomers incorporated in the hydrophobic parts their packing is tighter. These results already suggest that the architecture of the polymer chain can have a significant influence the formation of the particle core.

The NOESY spectra were also acquired, as shown in **Figure 30**, to investigate the interactions of the different proton moieties in samples which could provide additional information about the internal structure of the self-assembled particles.

For the PrOx-containing copolymers we observed strong interactions between the hydrophobic alkyl side chains (**P₁**, **P₂** and **P₃**) and their hydrophobic polymer backbone (**p**) and the same was analogously observed for the hydrophilic segments PMeOzi as an interaction between the methyl side chain moiety of MeOzi (**M**) and the polymer backbone (**m₁, m₂**).
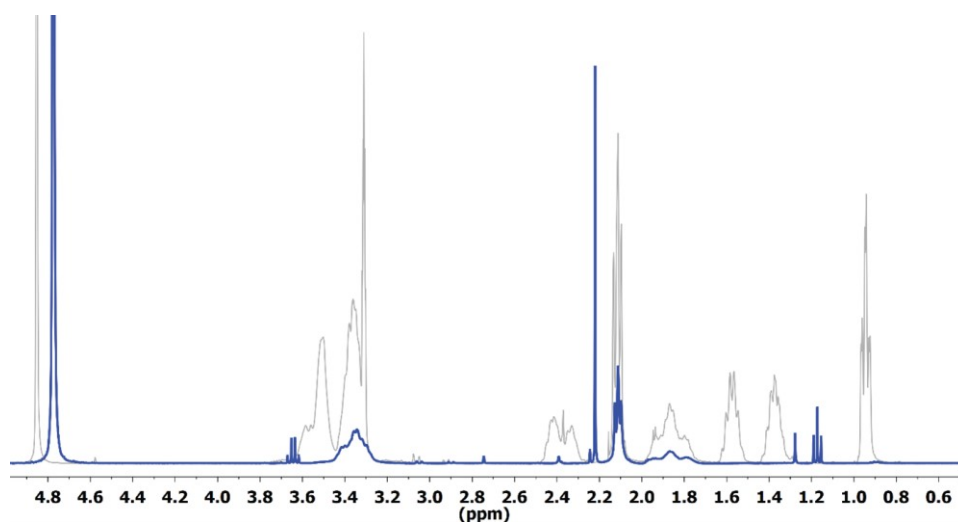
Figure 29 *Comparison of the ^{1}H NMR spectra of BB2-L particles in D_2O (blue) and a unimers in methanol-d4 (grey). The spectra were aligned (corresponding peaks have the same chemical shifts), and trace solvent peaks are not shown with their original amplitude to improve legibility. [27]*

An interesting observation was made of cross-interactions of the side chains and backbones of these monomers in both the gradient and block copolymers. This interaction was stronger in the gradient copolymers than the corresponding block copolymers, however it was still measurable for both architectures. This suggests some form of interaction between the hydrophilic and hydrophobic sections meaning that after self-assembly the polymer chains are arranged in such a structure where the hydrophilic monomers form a corona around the particle but also come to contact with the hydrophobic monomers aggregated into the particle core. These results give additional support to the proposed model of the observed particles as micelles and raspberry-like particles composed of them, as has been already suggested by results from SAXS experiments.

For the BuOx-containing copolymers the results are somewhat less rich on information as from the ^{1}H NMR spectra it seems that the majority of the hydrophobic monomer is solidified and dehydrated in the particle core. This is most likely also the reason why we only observe the interaction of the methyl moiety (**M**) and the hydrophilic backbone (**m₁, m₂**) in the NOESY spectrum of the block copolymer and there are no observed interactions with the hydrophobic monomer. The results of copolymer with gradient architecture indicate only a minor cross-interaction from MeOzi monomers with the hydrophobic BuOx monomers which could be ascribed to the presence of BuOx units in the MeOzi section. These observations indicate that the

68

BuOx-containing copolymers also phase separate and the hydrophobic part does so even more strongly than in the PrOx copolymers. The block architecture also increases this tendency.
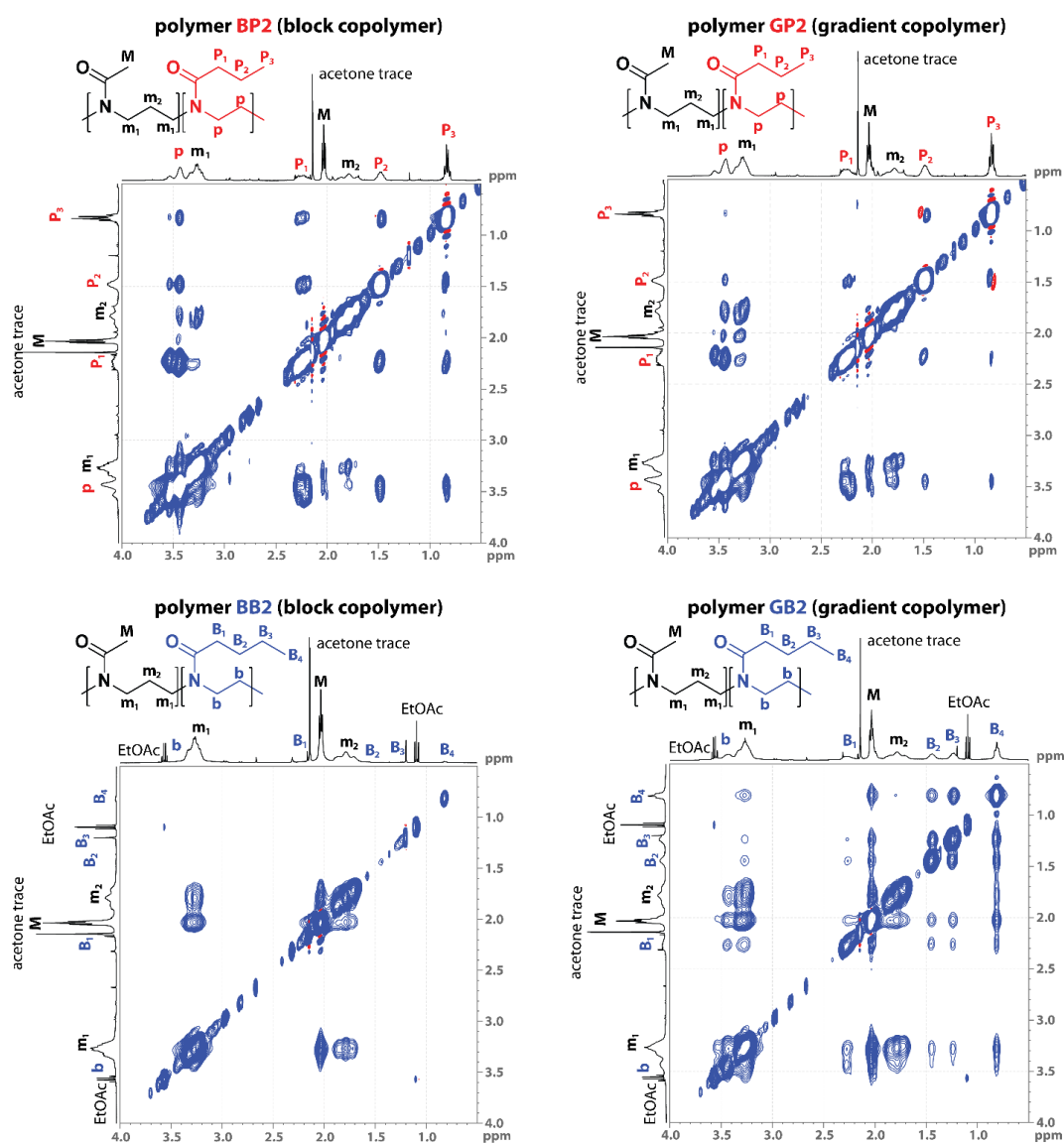
Figure 30 *Enlargement of the NOESY spectra of BP2-L (top left), GP2-L (top right), BB2-L (bottom left) and GB2-L (bottom right). Solvent peaks are not shown in their original amplitude to improve legibility. [27]*

The results obtained by the NMR experiments suggest that both block and gradient PrOx copolymers have a similar structure which could be described as a partially solidified core of PrOx monomers with a small number of MeOzi monomers mixed in and this core is surrounded by hydrophilic corona, primarily composed of the hydrophilic MeOzi monomers with the minor addition of hydrophobic PrOx monomers. The observations for the copolymers containing BuOx monomers are

mainly that their hydrophobic parts undergo a much more pronounced solidification and dehydration with some hydrophilic monomers also possibly entrapped in the core.

3.3.6 Bioapplication studies - CAC, drug loading and biocompatibility

To investigate the usefulness of the prepared polymer nanoparticles in biomedical applications a set of studies was carried out by a cooperating laboratory.

The critical association concentration, CAC, was determined for the selected samples using the 8-anilinonaphthalene-1-sulfonic acid as a solvatochromic fluorescent dye. These dyes change their emission spectrum based on the polarity of the environment so if their environment changes when the nanoparticles disassemble the change can be detected. [131] As discussed in the section 2.1.4 low CAC is crucial for practical biomedical applications as the self-assembled polymer nanoparticles need to withstand major dilution after entering the body without immediate disassembly so that they can reach their target tissues to deliver their drug payload there. The CAC values obtained from the experiments are listed in **Table 10**. If we consider human blood volume of approximately 4.5 l, 60 % of which is blood plasma, and typical expected dosage of the polymer drug delivery system in range of 500 mg to several grams, the CAC values are sufficiently low to assure stability of the nanoparticles.

CAC [mg·l^{-1}]	GP2	BP2	GB2	BB2
non-loaded	37.2 ± 2.3	36.7 ± 2.7	27.1 ± 1.1	10.2 ± 0.7
loaded	14.9 ± 1.8	7.8 ± 1.9	4.7 ± 1.3	1.7 ± 0.2

***Table 10** Critical association concentrations (CACs) for select copolymers. Data was collected from 5 independent experiments and results are shown as means with standard deviation. Adapted from [27].*

As expected, the PrOx-containing copolymers exhibited higher CAC than their BuOx counterparts which is most likely caused by the lower hydrophobicity of PrOx. The block copolymers expressed a lower CAC than the analogous gradient copolymers (both with and without the rifampicin present in the sample), as has been observed in other gradient and block PAOx systems as well. [28, 31] The loading of the rifampicin drug into the self-assembled nanoparticles significantly lowered the measured CAC values which is most likely caused by the stabilization of the particles through combination of hydrophobic interactions and hydrogen bonds between rifampicin molecule and copolymer chains as already discussed.

The drug loading properties of the prepared nanoparticles were also determined and their entrapment efficiency factor (f_{EE}) was calculated as shown in **Figure 31**. All the investigated samples expressed high loading capacities. There was no significant difference observed between the gradient and block copolymers, however there was some difference observed between the PrOx and BuOx-based copolymers. At rifampicin concentration equal to 20% of the concentration of the polymer in the sample the BuOx samples exhibited significantly higher f_{EE}. For other rifampicin concentrations no significant difference between the copolymers was observed leading to a conclusion they are mostly equivalent in their drug loading capacity.
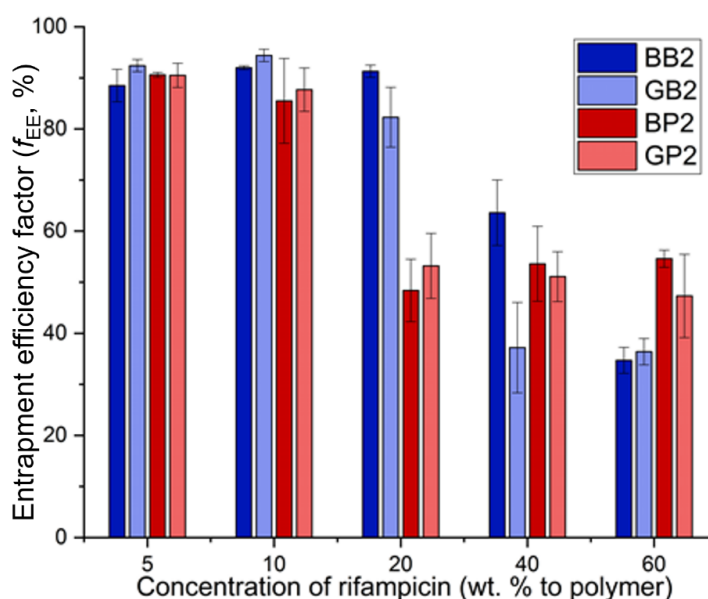
Figure 31 *Entrapment efficiency factor (f_{EE}) for copolymers BB2, GB2, BP2 and GP2 loaded with rifampicin. The data were collected in 2 independent experiments. The samples were prepared as 1.0 mg of polymer per 1 ml of PBS with varying amounts of rifampicin (0.05 to 0.60 mg). [27]*

Biocompatibility of the copolymers GB2, GP2, BB2 and BP2 was also investigated. Their cytotoxicity was tested on a set of cell lines and the experiments revealed no cytotoxicity from the copolymers within the tested concentration range (0.05 to 2.0 mg·ml^{-1}). Cellular uptake was tested on murine macrophage cells with fluorescent labelled copolymers and shown successful internalization of all prepared copolymer systems into the cells within 20 hours.

3.3.7 Summary comparison

This comprehensive study of PMeOzi:PPrOx/PBuOx copolymers with block and gradient monomer distributions uncovered important differences and similarities between them.

Both block and gradient copolymers showed capability of forming self-assembled nanoparticles in size range suitable for bioapplications. While the block copolymers showed slightly better stability the gradient copolymers were shown to be able to form particles with similar properties. The variation in the polymer architecture, the ratio of hydrophilic to thermoresponsive or hydrophobic monomers and the polymer chain length can all be used to fine-tune the properties of the formed particles.

The greatest advantage of the copolymers with gradient architecture remains their convenient and reproducible one-pot synthesis which gives better control over the resulting properties of the synthesized copolymers than the two-step synthesis of block copolymers.

Both PrOx and BuOx-based copolymers were shown to have their advantages and disadvantages. The PrOx-containing copolymers expressed thermoresponsive properties which could be used with advantage to design new stimuli-responsive self-assembled systems for drug delivery. During nanoparticle preparation they were easier to handle and less prone to macroprecipitation which was most likely due to their lower hydrophobicity because of the PrOx monomers, this however also led to them exhibiting higher CAC than their analogous BuOx-based copolymers. The lower CAC of the BuOx-containing copolymers is most likely caused by their greater hydrophobicity which stems from their different chemical composition. This also causes that they are not thermoresponsive in the classical sense and they require greater care during nanoprecipitation as they easily macroprecipitate.

The studies of biomedical applicability showed that all copolymers with 1:1 monomer ratio expressed good drug loading properties and low cytotoxicity. As such both PrOx and BuOx-based copolymers could be considered for further biomedical research based on the desired properties of the system. The gradient copolymers were shown to have somewhat different properties than their monomerically equivalent block copolymers, however these were still comparable and well suitable for potential biomedical applications.

4 Conclusion and future research prospects

4.1 Summary of results

In the research covered in this thesis:

•We confirmed the fluorinated block copolymers PHPMA-*block*-PDFEA and PMeOx-*block*-PDFEA were capable of self-assembly into nanoparticles based on the external stimulus of changing temperature. Depending on the ratio of lengths of their hydrophilic and thermoresponsive blocks they could be fine-tuned to provide the required thermal response at various temperatures.

•Through detailed analysis using scattering methods (DLS, SLS, SAXS and SANS) and additional methods such as TEM and NMR we were able to uncover the internal structure of the self-assembled nanoparticles formed by the fluorinated copolymers and confirm they form primarily highly swollen nanogel particles composed of interconnected hydrophobic network shielded by the hydrophilic blocks suspended in intraparticular aqueous environment. As the nanogel particles were shown to be advantageous for biomedical applications [4, 132-134] this further improves the prospects of the copolymers for practical use.

•We showed the nanoparticles were capable of providing measurable ^{19}F NMR signal under physiological conditions despite the fact that the blocks carrying the fluorine atoms become aggregated in the self-assembled particles and their ^{1}H NMR signal is strongly diminished. This is most likely connected to the different relaxation properties of the ^{1}H atoms and ^{19}F atoms in the thermoresponsive block.

•We thoroughly compared the properties of PMeOzi-PPrOx and PMeOzi-PBuOx copolymers with block and gradient chain architectures. We found both are capable of forming self-assembled nanoparticles and carrying loaded drug inside them. We identified the mechanism which supports their self-assembly as hydrogen bonding and hydrophobic interactions with the drug. We confirmed the PrOx-based copolymers exhibit reaction to external stimulus as a standard thermal response and self-assemble from freely dissolved unimers into micelle-like particles. On the other hand, most of the BuOx-based copolymers remained assembled across the whole investigated temperature range and exhibited a different type of thermal response in which the micelle-like particles aggregated to form larger assemblies which can be described with raspberry structure model. While gradient copolymers exhibited lower stability

as their CAC was systematically lower than for the block copolymers the difference was not so large that it would inhibit their usefulness in the biomedical applications and they were also much easier to synthesize.

4.2 Future research

Our vision for future research stems from results presented in this thesis. The systems we investigated were responsive to changes in temperature. In the future we would like to investigate multistimuli-responsive systems as well which would react also to changes in pH or increased concentration of reactive oxygen species in the environment. This could help with targeted release of the drugs they are carrying or it could be aimed at improving functional imaging where it would be possible to influence obtained MRI signal by an external stimulus.

Additionally, the fluorinated copolymers were investigated only as ^{19}F NMR contrast agents but their amphiphilic character could potentially enable them to also transport therapeutic molecules turning them from purely diagnostic tools to theranostics offering both therapeutic and diagnostic capabilities.

Our PMeOzi-PPrOx and PMeOzi-PBuOx systems were tested with rifampicin drug aimed at tuberculosis treatment. In the future we would like to expand this research over additional drugs to cover a wider range of illnesses these drug delivery systems could help to treat.

5 Bibliography

1. Gupta, S., et al., *Antimicrobial polymeric paints: An up-to-date review.* Polymers for Advanced Technologies, 2021. **32**(12): p. 4642-4662.
2. Gupta, V., et al., *Nanotechnology in Cosmetics and Cosmeceuticals-A Review of Latest Advancements.* Gels, 2022. **8**(3): p. 31.
3. Dong, X., et al., *Stimulus-responsive self-assembled prodrugs in cancer therapy.* Chemical Science, 2022. **13**(15): p. 4239-4269.
4. Seo, B.B., et al., *Injectable polymeric nanoparticle hydrogel system for long-term anti-inflammatory effect to treat osteoarthritis.* Bioactive Materials, 2022. **7**: p. 14-25.
5. Yang, Y., et al., *Inflammation-targeting polymeric nanoparticles deliver sparfloxacin and tacrolimus for combating acute lung sepsis.* Journal of Controlled Release, 2020. **321**: p. 463-474.
6. Ludwig, A., *The use of mucoadhesive polymers in ocular drug delivery.* Advanced Drug Delivery Reviews, 2005. **57**(11): p. 1595-1639.
7. Popovic, N. and P. Brundin, *Therapeutic potential of controlled drug delivery systems in neurodegenerative diseases.* International Journal of Pharmaceutics, 2006. **314**(2): p. 120-126.
8. Schlachetzki, F., et al., *Gene therapy of the brain - The trans-vascular approach.* Neurology, 2004. **62**(8): p. 1275-1281.
9. Kumar, M., et al., *Chitosan IFN-gamma-pDNA Nanoparticle (CIN) Therapy for Allergic Asthma.* Genet Vaccines Ther, 2003. **1**(1): p. 3.
10. Allen, T.M. and P.R. Cullis, *Drug delivery systems: entering the mainstream.* Science, 2004. **303**(5665): p. 1818-22.
11. Duncan, R., *The dawning era of polymer therapeutics.* Nat Rev Drug Discov, 2003. **2**(5): p. 347-60.
12. Tiwari, G., et al., *Drug delivery systems: An updated review.* Int J Pharm Investig, 2012. **2**(1): p. 2-11.
13. Doncom, K.E.B., et al., *Dispersity effects in polymer self-assemblies: a matter of hierarchical control.* Chem Soc Rev, 2017. **46**(14): p. 4119-4134.
14. Hruby, M., S.K. Filippov, and P. Stepanek, *Biomedical Application of Block Copolymers*, in *Macromolecular Self-Assembly*, L. Billon and O. Borisov, Editors. 2016, Wiley: Hoboken, New Jersey. p. 231-250.
15. Yadav, S., A.K. Sharma, and P. Kumar, *Nanoscale Self-Assembly for Therapeutic Delivery.* Front Bioeng Biotechnol, 2020. **8**: p. 127.
16. Hruby, M., *Self-assembly in Polymer Systems Inspired by Living Nature.* Chemicke Listy, 2018. **112**(5): p. 294-300.
17. Patist, A., et al., *Importance of micellar kinetics in relation to technological processes.* J Colloid Interface Sci, 2002. **245**(1): p. 1-15.
18. Zhang, Z., R. Ma, and L. Shi, *Cooperative macromolecular self-assembly toward polymeric assemblies with multiple and bioactive functions.* Acc Chem Res, 2014. **47**(4): p. 1426-37.
19. Sabin, J.R., *Hydrogen bonds involving sulfur .1. hydrogen sulfide dimer.* Journal of the American Chemical Society, 1971. **93**(15): p. 3613-&.
20. Chandler, D., *Interfaces and the driving force of hydrophobic assembly.* Nature, 2005. **437**(7059): p. 640-7.

21.   Hoa112008. *Space-filling model of the sodium dodecyl sulfate (SDS)*. 2021; Available from: https://commons.wikimedia.org/wiki/File:Sodium-dodecyl-sulfate-3D-vdW.png.

22.   Lindman, B.r. and P. Alexandridis, *Amphiphilic block copolymers : self-assembly and applications*. 1st ed. 2000, Amsterdam ; New YOrk: Elsevier. xii, 435 p.

23.   Mai, Y. and A. Eisenberg, *Self-assembly of block copolymers.* Chem Soc Rev, 2012. **41**(18): p. 5969-85.

24.   van Hest, J.C., et al., *Polystyrene-dendrimer amphiphilic block copolymers with a generation-dependent aggregation.* Science, 1995. **268**(5217): p. 1592-5.

25.   Zhang, L. and A. Eisenberg, *Multiple Morphologies of "Crew-Cut" Aggregates of Polystyrene-b-poly(acrylic acid) Block Copolymers.* Science, 1995. **268**(5218): p. 1728-31.

26.   Zhang, L., K. Yu, and A. Eisenberg, *Ion-Induced Morphological Changes in "Crew-Cut" Aggregates of Amphiphilic Block Copolymers.* Science, 1996. **272**(5269): p. 1777-9.

27.   Babuka, D., et al., *Self-Assembly, Drug Encapsulation, and Cellular Uptake of Block and Gradient Copolymers of 2-Methyl-2-oxazine and 2-n-Propyl/butyl-2-oxazoline.* Macromolecules, 2021. **54**(23): p. 10667-10681.

28.   Filippov, S.K., et al., *Block and Gradient Copoly(2-oxazoline) Micelles: Strikingly Different on the Inside.* Journal of Physical Chemistry Letters, 2017. **8**(16): p. 3800-3804.

29.   Hoogenboom, R., et al., *A schizophrenic gradient copolymer: switching and reversing poly(2-oxazoline) micelles based on UCST and subtle solvent changes.* Soft Matter, 2009. **5**(19): p. 3590-3592.

30.   Pakula, T. and K. Matyjaszewski, *Copolymers with controlled distribution of comonomers along the chain .1. Structure, thermodynamics and dynamic properties of gradient copolymers. Computer simulation.* Macromolecular Theory and Simulations, 1996. **5**(5): p. 987-1006.

31.   Sedlacek, O., et al., *Unexpected Reactivity Switch in the Statistical Copolymerization of 2-Oxazolines and 2-Oxazines Enabling the One-Step Synthesis of Amphiphilic Gradient Copolymers.* Journal of the American Chemical Society, 2019. **141**(24): p. 9617-9622.

32.   Verbraeken, B., et al., *The chemistry of poly(2-oxazoline)s.* European Polymer Journal, 2017. **88**: p. 451-469.

33.   Zaremski, M.Y., D.I. Kalugin, and V.B. Golubev, *Gradient copolymers: Synthesis, structure, and properties.* Polymer Science Series A, 2009. **51**(1): p. 103-122.

34.   Zhang, J., et al., *Asymmetric Copolymers: Synthesis, Properties, and Applications of Gradient and Other Partially Segregated Copolymers.* Macromol Rapid Commun, 2018. **39**(19): p. e1800357.

35.   Zhang, J.L., et al., *Effect of Hydrophilic Monomer Distribution on Self-Assembly of a pH-Responsive Copolymer: Spheres, Worms and Vesicles from a Single Copolymer Composition.* Angewandte Chemie-International Edition, 2021. **60**(9): p. 4925-4930.

36.   Zheng, C., *Gradient copolymer micelles: an introduction to structures as well as structural transitions.* Soft Matter, 2019. **15**(27): p. 5357-5370.

37.   Nyrkova, I.A. and A.N. Semenov, *On the theory of aggregation and micellization: PEO-PVP copolymer in water.* Faraday Discuss, 2005. **128**: p. 113-27.

38.   Israelachvili, J.N., D.J. Mitchell, and B.W. Ninham, *Theory of self-assembly of lipid bilayers and vesicles.* Biochim Biophys Acta, 1977. **470**(2): p. 185-201.

39.   Dionzou, M., et al., *Comparison of methods for the fabrication and the characterization of polymer self-assemblies: what are the important parameters?* Soft Matter, 2016. **12**(7): p. 2166-76.

40.   Lund, R., L. Willner, and D. Richter, *Kinetics of Block Copolymer Micelles Studied by Small-Angle Scattering Methods*, in *Controlled Polymerization and Polymeric Structures: Flow Microreactor Polymerization, Micelles Kinetics, Polypeptide Ordering, Light Emitting Nanostructures*, A. Abe, et al., Editors. 2013, Springer-Verlag Berlin: Berlin. p. 51-158.

41.   Desando, M.A. and L.W. Reeves, *The demicellization temperature of potassium n-octanoate in deuterium oxide as estimated from 1H and 13C nuclear magnetic resonance spectra.* Canadian Journal of Chemistry, 1986. **64**(9): p. 1817-1822.

42.   Nikoubashman, A. and A.Z. Panagiotopoulos, *Communication: Effect of solvophobic block length on critical micelle concentration in model surfactant systems.* Journal of Chemical Physics, 2014. **141**(4): p. 4.

43.   Cifuentes, A., J.L. Bernal, and J.C. DiezMasa, *Determination of critical micelle concentration values using capillary electrophoresis instrumentation.* Analytical Chemistry, 1997. **69**(20): p. 4271-4274.

44.   Khougaz, K., Z.S. Gao, and A. Eisenberg, *Determination of the critical micelle concentration of block-copolymer micelles by static light-scattering.* Macromolecules, 1994. **27**(22): p. 6341-6346.

45.   Chernitsky, E.A., V.V. Rozin, and O.A. Senkovich, *Influence of pH of the medium on parameters of detergent-induced hemolysis and vesiculation of erythrocytes.* Biologicheskie Membrany, 2000. **17**(4): p. 420-426.

46.   Hutin, A., *Application Notes -Method: 4. Measurement of Critical Micelle Concentration (CMC).* 2021.

47.   Hiemenz, P.C. and T. Lodge, *Polymer chemistry.* 2nd ed. 2007, Boca Raton: CRC Press. xvii, 587 p.

48.   Munk, P. and T.M. Aminabhavi, *Introduction to macromolecular science.* 2nd ed. 2002, New York: Wiley. xxi, 609 p.

49.   Kalogeras, I.M., *Glass-Transition Phenomena in Polymer Blends*, in *Encyclopedia of Polymer Blends: Volume 3: Structure*, A.I. Isayev, Editor. 2016, Wiley-VCH. p. 1-134.

50.   Van Der Haegen, R. and B.W. Ready, *4 - Phase Separation and Pulse-induced Critical Scattering*, in *Comprehensive Polymer Science and Supplements*, G. Allen and J.C. Bevington, Editors. 1989, Pergamon. p. 121-134.

51.   Liu, Y., et al., *pH-sensitive polymeric micelles triggered drug release for extracellular and intracellular drug targeting delivery.* Asian Journal of Pharmaceutical Sciences, 2013. **8**(3): p. 159-167.

52.   Zhang, Z., et al., *Magnetic resonance imaging-visible and pH-sensitive polymeric micelles for tumor targeted drug delivery.* J Biomed Nanotechnol, 2014. **10**(2): p. 216-26.

53.   Babuka, D., et al., *Internal Structure of Thermoresponsive Physically Crosslinked Nanogel of Poly N-(2-hydroxypropyl)methacrylamide -Block-*

Poly N-(2,2-difluoroethyl) acrylamide , Prominent F-19 MRI Tracer. Nanomaterials, 2020. **10**(11): p. 17.

54. Murthy, S.K., *Nanoparticles in modern medicine: state of the art and future challenges.* Int J Nanomedicine, 2007. **2**(2): p. 129-41.

55. Zhang, L., et al., *Nanoparticles in medicine: therapeutic applications and developments.* Clin Pharmacol Ther, 2008. **83**(5): p. 761-9.

56. Wilczewska, A.Z., et al., *Nanoparticles as drug delivery systems.* Pharmacological Reports, 2012. **64**(5): p. 1020-1037.

57. Edward, C., *Physicians' Cancer Chemotherapy Drug Manual 2021.* 2020: Jones & Bartlett Pub Inc.

58. Ahrens, E.T. and J. Zhong, *In vivo MRI cell tracking using perfluorocarbon probes and fluorine-19 detection.* Nmr in Biomedicine, 2013. **26**(7): p. 860-871.

59. Bouchoucha, M., et al., *Fluorinated Mesoporous Silica Nanoparticles for Binuclear Probes in (1)H and (19)F Magnetic Resonance Imaging.* Langmuir, 2017. **33**(40): p. 10531-10542.

60. Wolters, M., et al., *Clinical perspectives of hybrid proton-fluorine magnetic resonance imaging and spectroscopy.* Invest Radiol, 2013. **48**(5): p. 341-50.

61. Jirak, D., et al., *Fluorine polymer probes for magnetic resonance imaging: quo vadis?* Magnetic Resonance Materials in Physics Biology and Medicine, 2019. **32**(1): p. 173-185.

62. Kolouchova, K., et al., *Thermo- and ROS-Responsive Self-Assembled Polymer Nanoparticle Tracers for F-19 MRI Theranostics.* Biomacromolecules, 2021. **22**(6): p. 2325-2337.

63. Svec, P., et al., *Fluorinated Ferrocene Moieties as a Platform for Redox-Responsive Polymer F-19 MRI Theranostics.* Macromolecules, 2022. **55**(2): p. 658-671.

64. Blanco, E., H. Shen, and M. Ferrari, *Principles of nanoparticle design for overcoming biological barriers to drug delivery.* Nat Biotechnol, 2015. **33**(9): p. 941-51.

65. Yhee, J.Y., et al., *The EPR Effect in Cancer Therapy*, in *Cancer Targeted Drug Delivery: An Elusive Dream*, Y.H. Bae, R.J. Mrsny, and K. Park, Editors. 2013, Springer New York: New York, NY. p. 621-632.

66. Subhan, M.A., et al., *Recent Advances in Tumor Targeting via EPR Effect for Cancer Treatment.* Journal of Personalized Medicine, 2021. **11**(6): p. 27.

67. Wu, J., *The Enhanced Permeability and Retention (EPR) Effect: The Significance of the Concept and Methods to Enhance Its Application.* Journal of Personalized Medicine, 2021. **11**(8): p. 8.

68. Kalyane, D., et al., *Employment of enhanced permeability and retention effect (EPR): Nanoparticle-based precision tools for targeting of therapeutic and diagnostic agent in cancer.* Mater Sci Eng C Mater Biol Appl, 2019. **98**: p. 1252-1276.

69. Kutova, O.M., et al., *Targeted Delivery to Tumors: Multidirectional Strategies to Improve Treatment Efficiency.* Cancers (Basel), 2019. **11**(1).

70. Kataoka, K., A. Harada, and Y. Nagasaki, *Block copolymer micelles for drug delivery: design, characterization and biological significance.* Adv Drug Deliv Rev, 2001. **47**(1): p. 113-31.

71. Narayan, R., *Encyclopedia of biomedical engineering.* 2019, Amsterdam: Elsevier. 3 volumes.

72. Moreadith, R.W., et al., *Clinical development of a poly(2-oxazoline) (POZ) polymer therapeutic for the treatment of Parkinson's disease - Proof of concept of POZ as a versatile polymer platform for drug development in multiple therapeutic indications.* European Polymer Journal, 2017. **88**: p. 524-552.

73. Wyffels, L., et al., *muPET imaging of the pharmacokinetic behavior of medium and high molar mass (89)Zr-labeled poly(2-ethyl-2-oxazoline) in comparison to poly(ethylene glycol).* J Control Release, 2016. **235**: p. 63-71.

74. Longmire, M., P.L. Choyke, and H. Kobayashi, *Clearance properties of nano-sized particles and molecules as imaging agents: considerations and caveats.* Nanomedicine, 2008. **3**(5): p. 703-717.

75. Chen, B., et al., *The influence of polymer topology on pharmacokinetics: differences between cyclic and linear PEGylated poly(acrylic acid) comb polymers.* J Control Release, 2009. **140**(3): p. 203-9.

76. Osi, B., et al., *Pharmaceutical, biomedical and ophthalmic applications of biodegradable polymers (BDPs): literature and patent review.* Pharmaceutical Development and Technology: p. 16.

77. Parente, J.F., et al., *Biodegradable Polymers for Microencapsulation Systems.* Advances in Polymer Technology, 2022. **2022**: p. 43.

78. Pusey, P.N., *Introduction to Scattering Experiments*, in *Neutron, X-rays and Light Scattering Methods Applied to Soft Condensed Matter*, P. Lindner and T. Zemb, Editors. 2002, Elsevier: Amsterdam. p. 3-21.

79. Lindner, P. and T. Zemb, *Neutrons, X-rays, and light : scattering methods applied to soft condensed matter*. 1st ed. North-Holland delta series,. 2002, Amsterdam ; Boston: Elsevier. x, 541 p.

80. Patterson, J.P., et al., *The analysis of solution self-assembled polymeric nanomaterials.* Chem Soc Rev, 2014. **43**(8): p. 2412-25.

81. Tabatabai, A.P., *Small Angle Neutron Scattering Fundamentals*. Georgetown University, Department of Physics.

82. Richards, J.J., *Contrast Variation Small Angle Neutron Scattering-Identifying the Unique Fingerprints for the Structure of Proteins*. 2018, NCNR Summer School.

83. Brown, W., *Light scattering : principles and development*. Monographs on the physics and chemistry of materials. 1996, Oxford, New York: Clarendon Press; Oxford University Press. xvi, 528 p.

84. Schurtenberger, P., *Contrast and contrast variaion in neutron, X-ray and light scatering*, in *Neutron, X-rays and Light Scattering Methods Applied to Soft Condensed Matter*, P. Lindner and T. Zemb, Editors. 2002, Elsevier: Amsterdam.

85. 4LegsGood. *Graphic Explanation of a Zimm Plot*. 2001; Available from: https://commons.wikimedia.org/wiki/File:Graphic_Explanation_of_a_Zimm_Plot.jpg.

86. Hutchings, M.T., et al., *Introduction to the characterization of residual stress by neutron diffraction*. 2005, Boca Raton, FL: Taylor & Francis. 401 p.

87. Svergun, D.I., et al., *Small angle x-ray and neutron scattering from solutions of biological macromolecules*. First Edition. ed. IUCr texts on crystallography. 2013, Oxford: Oxford University Press. ix, 358 pages.

88. Schärtl, W., *Light scattering from polymer solutions and nanoparticle dispersions*. Springer laboratory manuals in polymer science. 2007, Berlin ; New York: Springer. xiv, 191 p.

89. Brown, W., *Dynamic light scattering : the method and some applications*. Monographs on the physics and chemistry of materials. 1993, Oxford England, New York: Clarendon Press ; Oxford University Press. xvi, 735 p.

90. Provencher, S.W., *A constrained regularization method for inverting data represented by linear algebraic or integral equations*. Computer Physics Communications, 1982. **27**(3): p. 213-227.

91. Provencher, S.W., *CONTIN - A general-purpose constrained regularization program for inverting noisy linear algebraic and integral equations*. Computer Physics Communications, 1982. **27**(3): p. 229-242.

92. Provencher, S.W. and P. Stepanek, *Global analysis of dynamic light scattering autocorrelation functions*. Particle & Particle Systems Characterization, 1996. **13**(5): p. 291-294.

93. Stetefeld, J., S.A. McKenna, and T.R. Patel, *Dynamic light scattering: a practical guide and applications in biomedical sciences*. Biophys Rev, 2016. **8**(4): p. 409-427.

94. Malvern, *Dynamic Light Scattering: An Introduction in 30 Minutes*. 2014, Malvern Panalytical.

95. Günther, H., *NMR Spectroscopy: Basic Principles, Concepts and Applications in Chemistry*. 2013: Wiley. 734.

96. Groborz, O., *Pharmacokinetics of Intramuscularly Administered Thermoresponsive Polyacrylamides*, in *Department of Organic Chemistry, Faculty of Science*. 2021, Charles University: Prague. p. 74.

97. Kolouchova, K. and O. Groborz, *Multiresponsive Polymer Tracers for F-19 MRI Based on Poly N-(2,2-difluoroethyl) Acrylamide*. Chemicke Listy, 2022. **116**(3): p. 180-186.

98. Kolouchova, K., et al., *Self-Assembled Thermoresponsive Polymeric Nanogels for F-19 MR Imaging*. Biomacromolecules, 2018. **19**(8): p. 3515-3524.

99. Sedlacek, O., et al., *Thermoresponsive Polymers for Nuclear Medicine: Which Polymer Is the Best?* Langmuir, 2016. **32**(24): p. 6115-22.

100. Lodge, T.P., et al., *Origins of anomalous micellization in diblock copolymer solutions*. Langmuir, 2003. **19**(6): p. 2103-2109.

101. Blanazs, A., S.P. Armes, and A.J. Ryan, *Self-Assembled Block Copolymer Aggregates: From Micelles to Vesicles and their Biological Applications*. Macromolecular Rapid Communications, 2009. **30**(4-5): p. 267-277.

102. Tahara, Y. and K. Akiyoshi, *Current advances in self-assembled nanogel delivery systems for immunotherapy*. Adv Drug Deliv Rev, 2015. **95**: p. 65-76.

103. Babuka, D., et al., *Investigation of the internal structure of thermoresponsive diblock poly(2-methyl-2-oxazoline)-b-poly N-(2,2-difluoroethyl)acrylamide copolymer nanoparticles*. European Polymer Journal, 2019. **121**: p. 8.

104. Sedlacek, O. and R. Hoogenboom, *Drug Delivery Systems Based on Poly(2-Oxazoline)s and Poly(2-Oxazine)s*. Advanced Therapeutics, 2020. **3**(1): p. 18.

105. Sedlacek, O., et al., *Poly(2-Oxazoline)s - Are They More Advantageous for Biomedical Applications Than Other Polymers?* Macromolecular Rapid Communications, 2012. **33**(19): p. 1648-1662.

106. Bauer, M., et al., *Poly(2-ethyl-2-oxazoline) as Alternative for the Stealth Polymer Poly(ethylene glycol): Comparison of in vitro Cytotoxicity and Hemocompatibility*. Macromolecular Bioscience, 2012. **12**(7): p. 986-998.

107.   de la Rosa, V.R., *Poly(2-oxazoline)s as materials for biomedical applications.* Journal of Materials Science-Materials in Medicine, 2014. **25**(5): p. 1211-1225.

108.   Harris, J.M., et al., *Tuning drug release from polyoxazoline-drug conjugates.* European Polymer Journal, 2019. **120**: p. 11.

109.   Lorson, T., et al., *Poly(2-oxazoline)s based biomaterials: A comprehensive and critical update.* Biomaterials, 2018. **178**: p. 204-280.

110.   Luxenhofer, R., et al., *Poly(2-oxazoline)s as Polymer Therapeutics.* Macromolecular Rapid Communications, 2012. **33**(19): p. 1613-1631.

111.   Pizzi, D., et al., *Poly(2-oxazoline) macromonomers as building blocks for functional and biocompatible polymer architectures.* European Polymer Journal, 2019. **121**: p. 17.

112.   Lubtow, M.M., et al., *Drug Specificity, Synergy and Antagonism in Ultrahigh Capacity Poly(2-oxazoline)/Poly(2-oxazine) based Formulations.* Journal of the American Chemical Society, 2017. **139**(32): p. 10980-10983.

113.   Morgese, G., et al., *Chemical Design of Non-Ionic Polymer Brushes as Biointerfaces: Poly(2-oxazine)s Outperform Both Poly(2-oxazoline)s and PEG.* Angewandte Chemie-International Edition, 2018. **57**(36): p. 11667-11672.

114.   Varanaraja, Z., J. Kim, and C.R. Becer, *Poly(2-oxazine)s: A comprehensive overview of the polymer structures, physical properties and applications.* European Polymer Journal, 2021. **147**: p. 11.

115.   Zahoranova, A. and R. Luxenhofer, *Poly(2-oxazoline)- and Poly(2-oxazine)-Based Self-Assemblies, Polyplexes, and Drug Nanoformulations-An Update.* Advanced Healthcare Materials, 2021. **10**(6): p. 27.

116.   Bobde, Y., S. Biswas, and B. Ghosh, *Current trends in the development of HPMA-based block copolymeric nanoparticles for their application in drug delivery.* European Polymer Journal, 2020. **139**: p. 19.

117.   Tucker, B.S. and B.S. Sumerlin, *Poly(N-(2-hydroxypropyl) methacrylamide)-based nanotherapeutics.* Polymer Chemistry, 2014. **5**(5): p. 1566-1572.

118.   Ma, L., L. Deng, and J. Chen, *Applications of poly(ethylene oxide) in controlled release tablet systems: a review.* Drug Dev Ind Pharm, 2014. **40**(7): p. 845-51.

119.   Dwivedi, R., et al., *Polycaprolactone as biomaterial for bone scaffolds: Review of literature.* J. Oral Biol. Craniofac. Res., 2020. **10**(1): p. 381-388.

120.   Guarino, V., et al., *Polycaprolactone: Synthesis, Properties, and Applications*, in *Encyclopedia of Polymer Science and Technology*. p. 1-36.

121.   De Stefano, V., S. Khan, and A. Tabada, *Applications of PLA in modern medicine.* Engineered Regeneration, 2020. **1**: p. 76-87.

122.   Rossi Sebastiano, M., et al., *Impact of Dynamically Exposed Polarity on Permeability and Solubility of Chameleonic Drugs Beyond the Rule of 5.* J Med Chem, 2018. **61**(9): p. 4189-4202.

123.   Mariappan, T.T., N. Sharda, and S. Singh, *Atypical Log D profile of rifampicin.* Indian J Pharm Sci, 2007. **69**(2): p. 197-201.

124.   Bianchi, A., et al., *Hierarchical Self-Assembly of PDMA-b-PS Chains into Granular Nanoparticles: Genesis and Fate.* Macromolecular Rapid Communications, 2014. **35**(23): p. 1994-1999.

125.   Otulakowski, L., et al., *Thermal Behaviour of Common Thermoresponsive Polymers in Phosphate Buffer and in Its Salt Solutions.* Polymers, 2021. **13**(1): p. 14.

126.   Doberenz, F., et al., *Thermoresponsive polymers and their biomedical application in tissue engineering - a review.* Journal of Materials Chemistry B, 2020. **8**(4): p. 607-628.

127.   Doucet, M., et al., *SasView version 4.2 (4.2.0).* 2018.

128.   Larson-Smith, K., A. Jackson, and D.C. Pozzo, *Small angle scattering model for Pickering emulsions and raspberry particles.* Journal of Colloid and Interface Science, 2010. **343**(1): p. 36-41.

129.   Franke, D. and D.I. Svergun, *DAMMIF, a program for rapid ab-initio shape determination in small-angle scattering.* Journal of Applied Crystallography, 2009. **42**: p. 342-346.

130.   Svergun, D.I., M.V. Petoukhov, and M.H.J. Koch, *Determination of domain structure of proteins from X-ray solution scattering.* Biophysical Journal, 2001. **80**(6): p. 2946-2953.

131.   Evans, N.A. and P.A. Hoyne, *A fluorochrome from aniline blue - structure, synthesis and fluorescence properties.* Australian Journal of Chemistry, 1982. **35**(12): p. 2572-2575.

132.   Yuki, Y., et al., *Nanogel-based antigen-delivery system for nasal vaccines.* Biotechnol Genet Eng Rev, 2013. **29**: p. 61-72.

133.   Nakahashi-Ouchida, R., Y. Yuki, and H. Kiyono, *Development of a nanogel-based nasal vaccine as a novel antigen delivery system.* Expert Review of Vaccines, 2017. **16**(12): p. 1231-1240.

134.   Hernandez-Adame, L., et al., *An overview of nanogel-based vaccines.* Expert Rev Vaccines, 2019. **18**(9): p. 951-968.

6 List of figures

7   List of tables

8 List of abbreviations

BuOx	2-butyl-2-oxazoline
CAC	critical association concentration
CMC	critical micelle concentration
CT	computed tomography
DLS	dynamic light scattering
DNA	deoxyribonucleic acid
DOSY	diffusion ordered spectroscopy
EPR	enhanced permeability and retention
FID	free induction decay
LCST	lower critical solution temperature
MALS	multi-angle light scattering
MeOzi	2-methyl-2-oxazine
MRI	magnetic resonance imaging
NMR	nuclear magnetic resonance
NOESY	nuclear Overhauser effect spectroscopy
PAOx	poly(2-alkyl-2-oxazoline)
PAOzi	poly(2-alkyl-2-oxazine)
PBS	phosphate buffered saline
PCL	poly(ε-caprolactone)
PDFEA	poly[N-(2,2-difluoroethyl)acrylamide]
PEO	poly(ethylene oxide)
PHPMA	poly[N-(2-hydroxypropyl) methacrylamide]
PLA	poly(lactic acid)
PMeOx	poly(2-methyl-2-oxazoline)
PrOx	2-propyl-2-oxazoline
SANS	small-angle neutron scattering
SAXS	small-angle X-ray scattering
SEC	size exclusion chromatography
SLD	scattering length density
SLS	static light scattering
TEM	transmission electron microscopy

UCST   upper critical solution temperature

9   List of publications

Publications included into this thesis:

Kolouchova, K.; Sedlacek, O.; Jirak, D.; **Babuka, D.**; Blahut, J.; Kotek, J.; Vit, M.; Trousil, J.; Konefal, R.; Janouskova O.; Podhorska, B.; Slouf, M.; Hruby, M. *Self-Assembled Thermoresponsive Polymeric Nanogels for ^{19}F MR Imaging.* Biomacromolecules **2018**, *19(8)*, 3515-3524.

Babuka, D.; Kolouchova, K.; Hruby, M.; Groborz, O.; Tosner, Z.; Zhigunov, A.; Stepanek, P. *Investigation of the internal structure of thermoresponsive diblock poly(2-methyl-2-oxazoline)-b-poly[N-(2,2-difluoroethyl)acrylamide]   copolymer nanoparticles.* European Polymer Journal **2019**, *121*, 8.

Babuka, D.*; Kolouchova, K.*; Groborz, O.; Tosner, Z.; Zhigunov, A.; Stepanek, P; Hruby, M. *Internal Structure of Thermoresponsive Physically Crosslinked Nanogel of Poly   N-(2-hydroxypropyl)methacrylamide   -Block-Poly   N-(2,2-difluoroethyl) acrylamide , Prominent F-19 MRI Tracer.* Nanomaterials **2020**, 10(11), 17.
*contributed equally

Babuka, D.; Kolouchova, K.; Loukotova, L.; Sedlacek, O.; Groborz, O.; Skarkova, A.; Zhigunov, A.; Pavlova, E.; Hoogenboom, R.; Hruby, M.; Stepanek, P. *Self-Assembly, Drug Encapsulation, and Cellular Uptake of Block and Gradient Copolymers   of   2-Methyl-2-oxazine   and   2-n-Propyl/butyl-2-oxazoline.* Macromolecules **2021**, 54(23), 10667-10681.

Publications not included into this thesis:

Plasek, J.; **Babuka, D.**; Gaskova, D.; Jancikova, I.; Zahumensky, J.; Hoefer, M. *A novel method for assessment of local pH in periplasmic space and of cell surface potential in yeast.* Journal of Bioenergetics and Biomembranes **2017**, 49(3), 273-279.

Plasek, J.; **Babuka, D.**; Hoefer, M. *H+ translocation by weak acid uncouplers is independent of H+ electrochemical gradient.* Journal of Bioenergetics and Biomembranes **2017**, 49(5), 391-397.

Jirak, D.; Galisova, A.; Kolouchova, K.; **Babuka, D.**; Hruby, M. *Fluorine polymer probes for magnetic resonance imaging: quo vadis?* Magnetic Resonance Materials in Physics Biology and Medicine **2019**, 32, 173-185.

Rohiwal, S.S.; Dvorakova, N.; Klima, J.; Vaskovicova, M.; Senigl, F.; Slouf, M.; Pavlova, E.; Stepanek, P.; **Babuka, D.**; Benes, H.; Ellederova, Z.; Stieger, K. *Polyethylenimine based magnetic nanoparticles mediated non-viral CRISPR/Cas9 system for genome editing.* Scientific Reports **2020**; 10(1), 12.

Kolouchova, K.; Lobaz, V.; Benes, H.; de la Rosa, V.R.; **Babuka, D.**; Svec, P.; Cernoch, P.; Hruby, M.; Hoogenboom, R.; Stepanek, P.; Groborz, O. *Thermoresponsive properties of polyacrylamides in physiological solutions.* Polymer Chemistry **2021**, 12(35), 5077-5084.

Contributions at conferences:

Babuka, D.; Hrubý, M.; Kolouchová, K.; Loukotová, L.; Sedláček, O. *Critical comparison of block and gradient amphiphilic copolymers for biomedical use.* Abstract book. Bordeaux: The Laboratoire de Chimie des Polymeres Organiques (LCPO), 2018. s. 292, Bordeaux Polymer Conference 2018. Bordeaux, France, **28.-31.5.2018**; poster.

Babuka, D.; Hrubý, M.; Kolouchová, K.; Loukotová, L.; Sedláček, O.; Šlouf, M.; Štěpánek, P.; Zhigunov, A. *Comparative analysis of block and gradient amphiphilic copolymers.* Sborník abstraktů. Praha: Ústav makromolekulární chemie AV ČR, v. v. i., 2018. s. 52. ISBN 978-80-85009-92-7. Česko-Slovenská konference POLYMERY 2018 /10./. Třešť, ČR, **2.-5.10.2018**; poster.

Babuka, D. also contributed to 7 other posters and presentations at conferences, which were presented by his colleagues.

10 Attachments

Attachment 1

Kolouchova, K**.;** Sedlacek, O.; Jirak, D.; **Babuka, D.**; Blahut, J.; Kotek, J.; Vit, M.; Trousil, J.; Konefal, R.; Janouskova O.; Podhorska, B.; Slouf, M.; Hruby, M. *Self-Assembled Thermoresponsive Polymeric Nanogels for ^{19}F MR Imaging.* Biomacromolecules **2018**, *19(8)*, 3515-3524.

Attachment 2

Babuka, D.; Kolouchova, K.; Hruby, M.; Groborz, O.; Tosner, Z.; Zhigunov, A.; Stepanek, P. *Investigation of the internal structure of thermoresponsive diblock poly(2-methyl-2-oxazoline)-b-poly[N-(2,2-difluoroethyl)acrylamide]   copolymer nanoparticles.* European Polymer Journal **2019**, *121*, 8.

Attachment 3

Babuka, D.; Kolouchova, K.; Groborz, O.; Tosner, Z.; Zhigunov, A.; Stepanek, P; Hruby, M. *Internal Structure of Thermoresponsive Physically Crosslinked Nanogel of Poly   N-(2-hydroxypropyl)methacrylamide   -Block-Poly   N-(2,2-difluoroethyl) acrylamide , Prominent F-19 MRI Tracer.* Nanomaterials **2020**, 10(11), 17.

Attachment 4

Babuka, D.; Kolouchova, K.; Loukotova, L.; Sedlacek, O.; Groborz, O.; Skarkova, A.; Zhigunov, A.; Pavlova, E.; Hoogenboom, R.; Hruby, M.; Stepanek, P. *Self-Assembly, Drug Encapsulation, and Cellular Uptake of Block and Gradient Copolymers   of   2-Methyl-2-oxazine   and   2-n-Propyl/butyl-2-oxazoline.* Macromolecules **2021**, 54(23), 10667-10681.